

https://dspace.org/

Alternating torsion and bending moment testing of a vehicle rim

Heukelman, B J; Heukelman, Brandon Jay

2020
https://hdl.handle.net/10539/31229

Downloaded from a DSpace repository. https://dspace.org/

Alternating Torsion and Bending Moment Testing of a Vehicle Rim

B.J. Heukelman

A dissertation submitted to the Faculty of Engineering and the Built Environment, University of the Witwatersrand, Johannesburg, in fulfilment of the requirements for the degree of Master of Science in Engineering.

Johannesburg, July 2020

Declaration

I declare that this dissertation is my own, unaided work, except where otherwise acknowledged. It is being submitted for the degree of Master of Science in Engineering in the University of the Witwatersrand, Johannesburg. It has not been submitted before for any degree or examination at any other university.

Signed this 27th day of July 2020



B.J. Heukelman

Acknowledgements

I would like to thank my supervisor Prof. Frank Kienhöfer for his constant support and advice, as well as my parents for giving me this opportunity to expand my knowledge.

Abstract

The automotive wheel is a fundamental vehicle component connecting the chassis to the road. Understanding the loading mechanism which leads to fatigue failure of a wheel is necessary to design light, safe wheels. This work characterised the strain along the length of spoke for various orientations with respect to the loading direction. Three wheel designs were tested according to the bending moment (cornering) and alternating torsion fatigue test specifications of the T$\ddot{U}$V and SAE. The results showed that the bending moment fatigue test (which reproduces the loading when cornering) is more critical than the alternating torsion fatigue test (which reproduces the loading when accelerating and decelerating). The bending moment load case produced strains that were on average 32 % higher than the torsion load case. The experimental results were compared to a finite element analysis (FEA) using commercial software (Ansys) and an analysis of the wheel which used Euler-Bernoulli beams and torsional elements to model the spokes of the wheel. The FEA underestimated the peak strains by 20 %, while the simplified model underestimated the peak strains by 30 %. Both the FEA and simplified model followed the same trend seen in the experimental results. The simplified model was further used to investigate the effect of spoke arrangement on the wheel's efficiency (i.e. the safety factor of the wheel normalised by the mass of the wheel). The model showed that increasing the number of spokes as well as increasing the angle of spoke to the radial increases the factor of safety (even after normalised with respect to mass).

Contents

Declaration i

Acknowledgements ii

Abstract iii

Contents iv

List of Figures vii

List of Tables ix

1 Introduction 1

1.1 Background 1

1.2 Blackstone Tek 2

1.3 Literature Review 2

2 Objectives 5

3 Apparatus 6

3.1 Test Specimens 6

3.2 Load Case Description 8

3.3 Test Rig Description 8
3.4 Instrumentation 9
3.5 Applied Loads 11
3.6 Strain Gauge Locations 13

4 Experimental Results **16**

4.1 Linear Strain Relationship 16
4.2 Repeatability of Experimental Results 16
4.3 Strain Distribution along Spoke Length 19
4.4 Strain Distribution with Orientation 20

5 Finite Element Analysis **27**

5.1 Finite Element Modelling Details 27
5.2 Investigation of Mesh Independence 28
5.3 Investigation of Boundary Conditions 30
5.4 Simulation Results 33

6 Simplified Model **36**

6.1 Required Inputs 37
6.2 The Euler-Bernoulli Beam 38
6.3 Global Stiffness Matrix 41
6.4 Force Vector and Finite Element Solution 42
6.5 Strain Calculation 42
6.6 Stress Calculation 44

7 Insights from the Simplified Model **46**

7.1 Comparison with Experimental Results 46

7.2 Comparison with an Idealised Wheel 51

7.3 Using the Simplified Model to Develop Insight into Wheel Design 52

7.4 Comparison of the Alternating Torsion, Bending Moment and Radial Fatigue Tests 59

8 Conclusions **61**

9 Recommendations **63**

A MatLab Code **66**

List of Figures

3.1 Marchesini M9RS ORW 6

3.2 Offset direction of motorcycle wheel 7

3.3 Marchesini 5 spoke CRW 7

3.4 Marchesini M7RR FW 7

3.5 Bending stiffness test rig 10

3.6 Torsional stiffness test rig 10

3.7 Strain gauge locations 14

4.1 Strain versus load for bending load 17

4.2 Strain versus load for torsional load 17

4.3 Relative orientations of primary and secondary spokes of 9 spoke ORW . . . 18

4.4 Strain versus radial position under bending load 21

4.5 Strain versus radial position under torsional load 22

4.6 Strain versus spoke orientation under bending load 24

4.7 Strain versus spoke orientation under torsional load 26

5.1 Geometry used in mesh independence study 28

5.2 Strain and element quality versus number of elements 29

5.3 Simplified boundary conditions 31

5.4 Full test rig simulation with connections 31

5.5 Finite element strain and experimentally-measured strain versus spoke orientation under bending load 34

5.6 Finite element strain and experimentally-measured strain versus spoke orientation under torsional load 35

6.1 Simplified model data flow 36

6.2 Simplified model coordinate system 37

6.3 3D Euler-Bernoulli beam element 39

6.4 Kinematic constraints for a Euler-Bernoulli beam 43

7.1 Diagram of elements and nodes of simplified model 47

7.2 Strain comparison versus spoke orientation under bending load 49

7.3 Strain comparison versus spoke orientation under torsional load 50

7.4 Idealised straight spoke wheel 51

7.5 Comparison of simplified model to idealised spoke FEA results 53

7.6 The effect of the number of spokes in the simplified model 54

7.7 The effect of the inner hub diameter in the simplified model 56

7.8 The effect of the spoke angle (β) in the simplified model 57

7.9 Diagram of elements and nodes of simplified model for different spoke angles 58

7.10 Strain versus spoke orientation for differing load cases 60

List of Tables

3.1 Wheel specimen details 8

3.2 Strain gauge properties 11

3.3 Load cell specifications 11

3.4 Strain gauge radial coordinate under bending load 14

3.5 Strain gauge radial coordinate under torsional load 15

4.1 Gradient of the strain along the length of the spoke 20

5.1 Material properties for FEA 27

5.2 Contacts in linear and non-linear simulation 32

5.3 Boundary condition comparison 32

6.1 Strength properties of materials 38

7.1 Critical wheel geometry 46

7.2 Required fatigue wheel loads 59

1 Introduction

1.1 Background

The automotive industry is driven to design lighter components so as to reduce fuel consumption and emissions. Designing to the limit necessitates a better understanding of the loading mechanisms of automotive components. Wheels are an extremely important component because they are the only load path between the tyre-road contact patch and the vehicle body. Large cornering, accelerating and decelerating forces are directed through the wheel. Reducing the mass and spinning inertia of rims can increase the vehicle efficiency but sufficient material is required to ensure the wheel can withstand the cornering, accelerating and decelerating loads without failure.

The failure of a wheel will cause a catastrophic and possibly fatal accident. Codes of practice, developed by the TÜV (Technischer Überwachungsverein - Technical Inspection Association)[1] and the SAE (Society of Automotive Engineers)[2], govern wheel design to reduce the risk of wheel failure. The codes specify laboratory tests as a proxy for the representative load cases experienced in the field. Impact tests, with the wheel and tyre mounted at 13° [3] and 90° [4], drop a specified weight on the wheel and tyre to replicate the loading case of hitting a pavement or pothole. The radial fatigue, the alternating torsion and bending moment (or dynamic cornering) fatigue [2, 1, 4] tests reproduce the load cases of straightline driving, accelerating and decelerating, and cornering of the vehicle respectively.

According to Wang et al. "*If the wheel passes the dynamic cornering fatigue test, it has a good chance of passing all other required durability tests*" [5]. This shows that the dynamic cornering fatigue test should be the primary focus of any wheel design investigation. Thus, the wheel's response to the loads induced by the dynamic cornering fatigue test were replicated in the experimental tests. Additionally, the alternating torsion fatigue test was also deemed necessary to investigate because of the relatively few studies investigating this fatigue test. Thus, similarly, the wheel's response caused by the loads induced by the alternating torsion

fatigue test were also replicated experimentally. Other fatigue load cases, that were less critical, were only examined through FEA and the simplified model.

The current wheel design approach is as follows: concepts are developed, the performance of the wheel may be simulated using FEA, a prototype is developed and tested according to the codes of practice, and finally if the wheel passes the testing, the wheel is manufactured [6]. This approach makes no effort to analyse the physics of the wheel failure mechanism. The approach relies heavily on the designer having expert knowledge and a feel for what will pass the required testing or relies heavily on expensive FEA software.

This study develops a simplified model of the wheel using Euler Bernoulli for beams and torsional elements to better understand the loading, strains and fatigue failure of wheels. This is compared to experimental and FEA results to provide some understanding of the major design features in a wheel design.

1.2 Blackstone Tek

Blackstone Tek (BST) is currently the largest producer of composite wheels for motorcycles in the world. BST develops and tests all its wheel designs in-house. Thus, they have a large amount of test data on wheel designs and a well developed test procedure. They also test competitor's wheels to find possible improvements in their own design.

BST supplied the necessary test samples and equipment required to preform this study.

1.3 Literature Review

As discussed in Section 1.1, this study will focus on the bending moment fatigue and alternating torsion fatigue tests. The following section will review relevant literature on these tests.

Bending Moment Fatigue Test

Karandikar and Fuchs [7] developed a computer-based design framework that utilises finite element results as an input to a pre-existing fatigue life computation program. The program predicted fatigue life in the same order of magnitude, but always below the experimental results. It was reasoned that the crack was allowed to propagate until it was visible in

the experiment, whereas the computed results only measured the fatigue life until the crack initiated.

Kocabicak and Firat [8] created a biaxial-stressed analytical model, using the total deformation theory of plasticity, that solved for the fatigue life of the wheel. The model correctly predicted the fatigue life with an 11% error when using computed strains as an input. However, the model still requires the elastic strains from either a finite element analysis or experimental measurement.

Raju et al. [9] used a purely finite element method to predict the fatigue life of an aluminium wheel under a bending moment load. It was concluded that there was a significant difference between experimental and computed results. The study proposed a conservative safety factor of 2.0 when predicting fatigue life under bending moment loads.

Shang et al. [10] advanced the work of Raju, by developing a post processor for a finite element analysis. The post processor predicted the fatigue factor of safety for each finite element. The multi-axial von Mises equivalent stress was used as an input into the widely accepted Goodman relationship. A weakness of this study was that the validation consisted only of comparing the crack location of the experiment with the location of the lowest safety factor in the finite element analysis. The model also requires the elastic strains from the finite element analysis to be determined.

Zheng et al. [11] expanded on Kocabicak and Firat's analytical model using a multi-axial stress model to determine when a crack is initiated, and predict the number of cycles until fatigue failure. They compared a variety of established methods to model the multi-axial stress. The Brown-Miller model was found to be the most accurate with a 12% error when compared to the experimental results. Again, the model requires the elastic strains from the finite element analysis to be determined.

The reviewed studies can accurately predict the fatigue life of a wheel, but all the methods require finite element analysis as an input to the respectively developed fatigue models. The finite element analysis requires time to build a three-dimensional CAD model and to rerun an analysis if any geometry changes are made. It is possible to improve these studies by developing a method that determines the stresses and strains in the spokes of a wheel without the use of a finite element method.

Alternating Torsion Fatigue Test

At present no studies have investigated and modelled a wheel in an alternating torsion test. It is possible that many researchers have the opinion of Wang [5] and Riesner [12], in Section 1.1, that only the dynamic cornering fatigue test is of primary concern. Experimental proof published in this study that the dynamic cornering fatigue test is critical would validate the statements of Wang and Kieser.

There exists a research gap within the literature to present a finite element model of a wheel loaded in an alternating torsion test and to compare the FEA results to experimentally determined strains. The experimental and FEA results could be used to confirm that the dynamic cornering fatigue test is more critical than the alternating torsion fatigue test.

2 Objectives

The objectives of this research are to:

- Characterise the strain response within the spoke of a wheel during a bending moment and torsional load case.
- Develop a simplified model of the wheel to better understand the loading, strains and fatigue failure of the wheels.
- Confirm and determine to what extent the bending moment fatigue test is more critical than the alternating torsion test.

3 Apparatus

3.1 Test Specimens

Three motorcycle wheels were tested. The specimens were pre-owned but in good working condition, with no damage. The wheel designs included the three types of wheels commonly seen in the motorcycle industry: offset rear wheel (ORW), conventional rear wheel (CRW), and front wheel (FW). The details of each wheel specimen are listed in Table 3.1.

The first specimen, a Marchesini M9RS ORW 9 spoke ORW, is shown in Figure 3.1. The wheel is currently used on the Ducati 1199/1299 Panigale superbike. The wheel is made from forged magnesium. This wheel is the cutting-edge of wheel design as it is one of the lightest magnesium wheels currently available on any mass produced motorcycle.

As seen in Figure 3.2, the positive offset position of the mounting face increases the moment arm length, thus increases the bending moment that the wheel experiences during cornering and torsional loading. This increased loading must be accommodated in analytical and computer simulations. The spoke configuration is in a three-pronged complex geometry. The spokes have a typical I-beam cross section, but with a high change in the spoke's cross-section along the length of the spoke.



Figure 3.1: Marchesini M9RS ORW

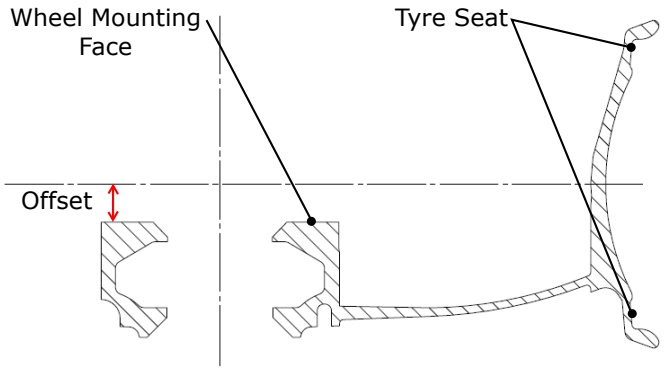


Figure 3.2: Offset direction of motorcycle wheel



Figure 3.3: Marchesini 5 spoke CRW



Figure 3.4: Marchesini M7RR FW

Marchesini's CRW has 5 equally spaced spokes at a slanted angle, as seen in Figure 3.3. This wheel is an older design and was manufactured from aluminium. The wheel first appeared on the 1997 Ducati 900SS/SP superbike. The spokes are tangential to the centre hub and have a U-channel cross section. The cross-section of these spokes are nearly constant along the length of the spoke.

To further examine the cutting-edge of wheel design, Marchesini M7RR Genesis FW (see Figure 3.4) was tested. This wheel is an uncommon size that is used for racing only. This wheel is made from forged magnesium and uses seven curved slanted spokes. The spokes are tangential to the centre hub and have a U-beam cross section. The spoke's cross section has a slight change along its length. Further complexity in the geometry is due to the spoke being curved.

Table 3.1: Wheel specimen details

Wheel Description	Wheel Size	Maximum Tyre Size	Offset	Material
9 Split Spoke ORW	17 x 6.00	190/60 R 17	20 mm	Forged Magnesium
5 Slanted Spoke CRW	17 x 5.50	190/60 R 17	0 mm	Cast Aluminium
7 Slanted Spoke FW	16 x 4.50	160/80 R 16	0 mm	Forged Magnesium

3.2 Load Case Description

The test standards for motorcycle wheels, as described in Section 1.1, require three fatigue tests and one impact test. The focus of this study is on the bending moment fatigue test that is said to be the most severe load case and the alternating torsion test that has received limited research.

Testing experience at BST has shown that the radial impact strength of a wheel is dependent on the material properties, shape and thicknesses of the outer wheel profile. Furthermore, the radial impact test is highly dependent on the tyre properties. The tyre is a highly non-linear system, and modelling tyre properties was not in the scope of this research. As discussed in the literature survey, the radial fatigue test is the least severe of the three tests. This load case was not experimentally tested, but the severity of radial loading is quantified in Section 7.4.

Static tests, as described in the following section, were performed instead of fatigue tests. Static tests allow for strain measurements while not permanently damaging the wheel, as these wheels were on loan from BST. The static tests are able to characterise the strains in the spoke more easily than the dynamic fatigue tests; allowing the dynamic cornering fatigue test strains to be synthesized from the static results if required.

3.3 Test Rig Description

Two test rigs were used to statically load the wheel in either torsion or bending, as described below. The bending stiffness test rig is shown in Figure 3.5 and the torsional stiffness test rig is shown in Figure 3.6. The test rigs generate a static load equivalent to the maximum dynamic load of the bending moment fatigue and alternating torsion fatigue test.

The hydraulic ram creates a force, measured by the load cell, through different load arms. The load arm changes depending on the type of moment that is required. The hydraulic ram can only contract, and has a maximum force of 10 tonnes (equivalent to 95.1 kN). The force

in the ram is manually adjusted by a hand pump until the correct load is displayed on the load cell output.

In the bending stiffness rig, the load arm connects to a 40 mm diameter axle. The wheel has spacers fitted in the bearing housing with a 40 mm internal diameter. An axle nut is tightened to the wheel manufacturer's recommended torque setting.

The bending moment in Figure 3.5 is not a pure couple, since it is generated by a remote force. The components of force acting at the centre of the wheel have a radial and axial component. The bending moment is equal to the radial force multiplied by the moment arm length.

In the torsional stiffness rig, the load arm connects to an adapter plate that has the same bolt pattern as the wheel load arm. The load arm uses 6 M8x1.25 bolts on a PCD of 168 mm. The load cell connects to the ram through a linear bearing. The force in Figure 3.6 has additional components acting at the wheel centre. The linear bearing ensures that the force is horizontal and two moments are generated. The intended torque and an overturning moment. The overturning moment is minimized by adjusting the linear bearings height to the wheel's centre.

On both test rigs, two dial gauges are used to measure displacement. The first dial gauge is placed at the hub and measures the translation of the hub in the direction of the force. The second dial gauge is placed at a known point along the load arm. The displacements are used to calculate the rotation of the load arm.

With a known moment applied to the hub and a calculated rotation on the load arm, the bending and torsional stiffness of the wheel can be calculated in $N \cdot m/^{\circ}$.

3.4 Instrumentation

The strains along the spoke were measure using general purpose foil strain gauges manufactured by Kyowa (see Table 3.2). The strain gauges were positioned in areas where maximum strain was expected; at a maximum distance away from the neutral axis and orientated in the expected principal stress direction.

Each strain gauge was connected to a National Instruments SCXI-1520 strain gauge card via SCXI-1314 terminal block using twisted three core shielded cable. This minimizes the adverse effect of temperature change on the strain measurement, provided that the leads are

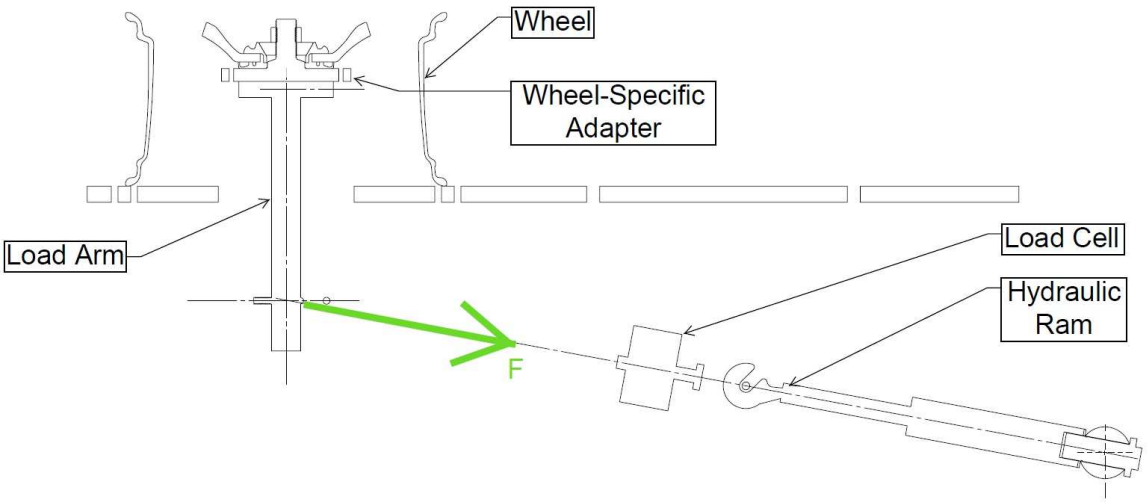


Figure 3.5: Bending stiffness test rig

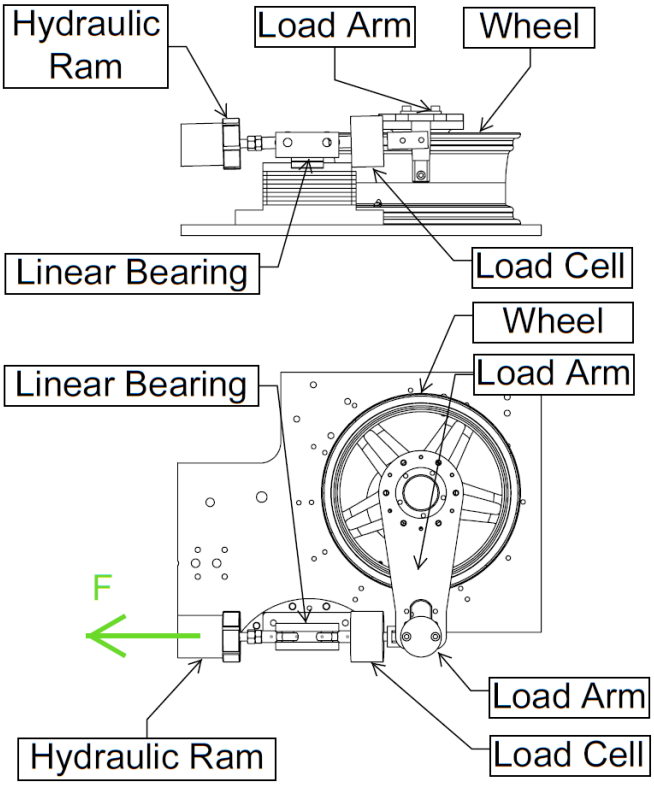


Figure 3.6: Torsional stiffness test rig

Table 3.2: Strain gauge properties

Name	KFG-5-120-C1-23
Length	5 mm
Gauge Factor	$2.12 \pm 1.0\%$
Electrical Resistance	$119.8 \pm 0.2\ \Omega$
Thermal Expansion Coefficient	23.4 $PPM/°C$

the same type, length, and cross-section. The lead wires are relatively short ($\leq$ 1.5 m) so that the gauge factor is not altered [13].

A National Instruments SCXI-1000 chassis and SCXI-1600 USB control module were used to import the measured strains onto a PC running LabView. The strain gauge card has eight channels. The card provides the Wheatstone bridge and shunt calibration for the strain gauges. Bridge completion is provided by a socketed 120 Ω resistor inside the terminal block. The data was recorded in a TDMS file format and imported into MATLAB for further post-processing.

A dual stud-mount load cell, manufactured by DPM, was used to measure the load placed on the moment arm. It has a range of 5 tonne and can operate in either tension or compression. For specifications see Table 3.3. The load cell was connected to a programmable load cell indicator, which has a 20-bit analogue to digital converter and a 5 $\frac{1}{2}$ digit display.

Table 3.3: Load cell specifications

Specification	Value
Uncertainty	$\pm 1\ kg$
Rated Output	2 mV/V *nominal*
Compensated Temperature Range	$16 - 70\ °C$
Nominal Resistance	350 Ω
Excitation Voltage	10 VDC

3.5 Applied Loads

The manufacturer's design loads of the tested wheels were not known, however the specific static load rating for each wheel was known. Furthermore, each wheel conforms to the International Standards Organisation (ISO) 8644:2006 wheel standard [4]. This standard specifies the required fatigue performance for a given static load rating when subjected to bending moment (dynamic cornering) and torsional loading.

Equation 3.1 calculates the bending moment and Equation 3.2 calculates the torsional moment that a wheel is required to withstand under fatigue loading according to ISO 8644:2006. In this study, the wheels were statically loaded at five incrementally increasing loads up to a maximum load of 150 % of the load calculated in Equation 3.1 and 3.2.

$$M_B = 0.7 \times \mu \times F_v \times R \tag{3.1}$$

$$M_T = F_v \times R \tag{3.2}$$

Where

M_B	=	Bending moment applied, in $N \cdot m$.
μ	=	Coefficient of friction, equal to 0.7 in ISO 8644:2006.
F_v	=	Static load rating of the wheel, in N.
R	=	Maximum in-service tyre radius of wheel, in m.
M_T	=	Torsional moment applied, in $N \cdot m$.

Each set of five incrementally increasing load was repeated three times.The wheel's orientation was then rotated by 60° and the testing repeated 6 times. This procedure was conducted for the bending moment and torsion loads on all the wheels.

By measuring the strains at five incrementally increasing loads, it could be confirmed that the wheels were loaded only in the linear elastic region of the material.

3.6 Strain Gauge Locations

The strain gauges were positioned such that they would be located on the surface of the spoke which had the highest amount of strain. The surface of the spoke that had the highest strain was the surface that was furthest away from the neutral axis of a spoke. However, the neutral axis on an individual spoke for the torsional load case and the bending load case were at different locations, hence the ideal surface to mount the strain gauges were different. Thus, two sets of strain gauges were used, depending on the load case.

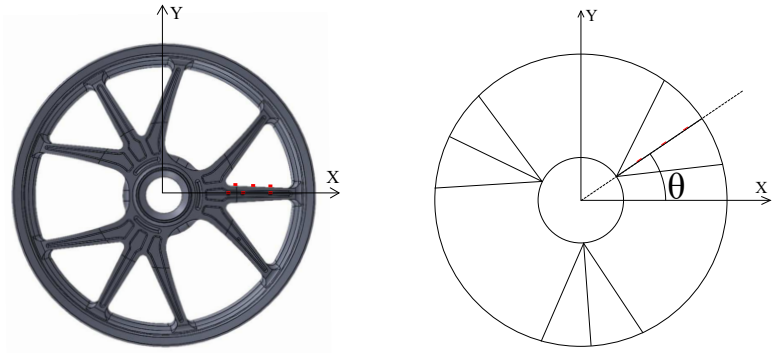
Three strain gauges were placed along the longitudinal axis of a single spoke. The centre strain gauge was a 3-way rosette. This allowed the full strain tensor at this point to be determined.

The location of the strain gauges on the 9 spoke ORW, 5 spoke CRW and 7 spoke FW is seen in Figures 3.7. In Figure 3.7 there were two images for each wheel. The left shows an image of the CAD, with the primary spoke's orientation at $\theta = 0°$. The right shows a diagram of the spoke geometry, with the primary spoke's orientation at some arbitrary angle θ. The global coordinate system (X, Y, Z) was shown with Z (the rolling axis) coming out of the page to form a right hand coordinate system. The spoke with strain gauges mounted on was referred to as the primary spoke.

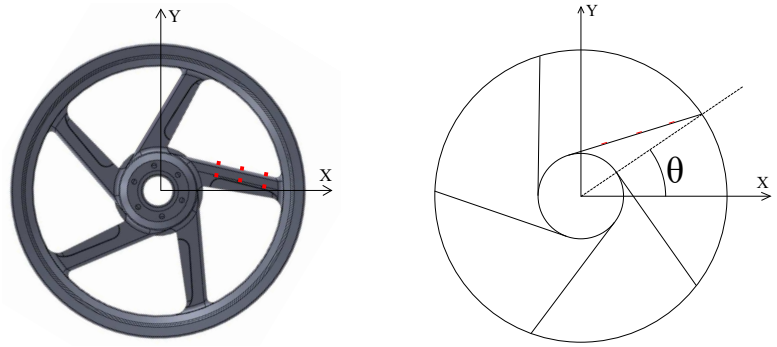
The local coordinate system $(x_n, y_n, z_n,\ n \in [1..N])$ of each spoke was located at the intersection of the inner hub and the spoke. Where N was equal to the number of spokes, and the primary spoke was $n = 1$. The local x axis followed the spoke's direction towards the outer rim and the local z axis remained parallel to the global Z axis. Then the local y axis was in such a direction to create a right hand coordinate system.

The local x coordinate of each strain gauge is listed in Table 3.4 for the bending load case, and Table 3.5 for the torsional load case.

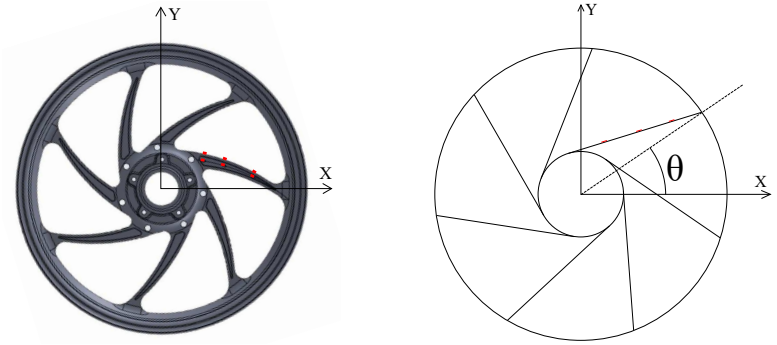
The remaining channels allowed for the verification of the primary spoke's strain measurement, because only five of the possible eight channels were used. The remaining three channels were filled with three single strain gauges, that were placed on a secondary spoke as to provide confidence in the data. These strain gauges were placed at the same radial coordinate as the primary strain gauges. Thus, a strain from the secondary and primary spoke may be compared when the orientation of the spoke is the same as discussed in Section 4.2.



(a) 9 Spoke ORW



b) 5 Spoke CRW



(c) 7 Spoke FW

Figure 3.7: Strain gauge locations and orientations of spokes with reference to global coordinate system for:
(a) 9 spoke ORW
(b) 5 spoke CRW
(c) 7 spoke FW

Table 3.4: Strain gauge radial coordinate under bending load

	5 Spoke CRW	7 Spoke FW	9 Split Spoke ORW
Inner Strain Gauge	82 mm	72 mm	95 mm
Middle Strain Gauge	125 mm	102 mm	117 mm
Outer Strain Gauge	162 mm	142 mm	158 mm

Table 3.5: Strain gauge radial coordinate under torsional load

	5 Spoke CRW	7 Spoke FW	9 Split Spoke ORW
Inner Strain Gauge	72 mm	83 mm	116 mm
Middle Strain Gauge	123 mm	112 mm	135 mm
Outer Strain Gauge	157 mm	145 mm	166 mm

4 Experimental Results

4.1 Linear Strain Relationship

The strain versus moment results for the 5 spoke CRW (which is representative of all three wheel designs) is shown in Figure 4.1, while the same wheel under torsional loading is shown for Figure 4.2. The orientation of the wheel is $\theta = 45°$ and $\theta = 60°$ for the bending and torsional load case, respectively. The moment is calculated from the amount of force applied multiplied by the length of moment arm, as seen in Section 3.3 and 3.5.

A linear regression line was fitted to each data set, with the y-intercept set to zero. The R-squared values were averaged across the three wheel samples to give an indication of the goodness of fit of the data to a straight line: 0.9756 for the bending load case and 0.9954 for the torsional load case.

The values close to unity indicate a strong linear relationship (no plastic deformation) and suggest the results are accurate and repeatable.

4.2 Repeatability of Experimental Results

The repeatability of the experimental results were examined by comparing the strain from the primary spoke and secondary spoke when they were in the same orientation and under the same load. Each wheel was rotated by 60° to its next orientation, thus wheels had their secondary spoke in the same position as their primary spoke.

For example, the 9 spoke ORW seen in Figure 4.3 had strain gauges on spoke 1 and spoke 2. When spoke 1 was at $\theta_1 = 120°$, the spoke 2 would be at $\theta_2 = 240°$. After four rotations of 60°, spoke 2 would be at $\theta_2 = 120°$ and the strain from spoke 2 may be were compared to the strain measured from spoke 1 when $\theta_1 = 120°$.

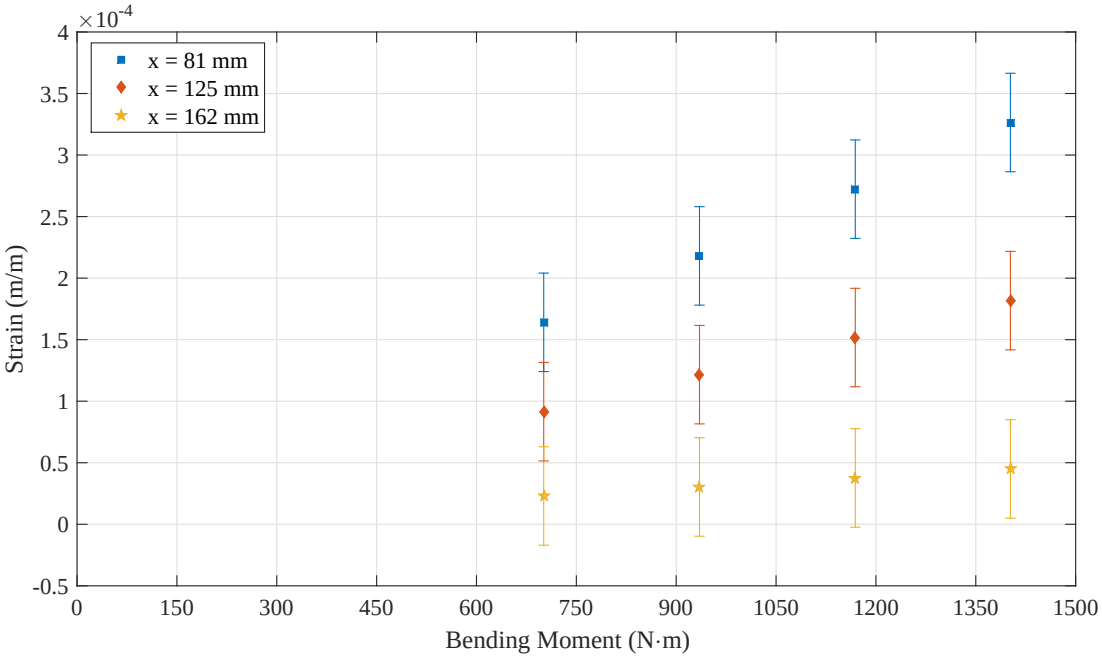


Figure 4.1: Strain versus load for 5 Spoke CRW under bending load case with $\theta = 45°$

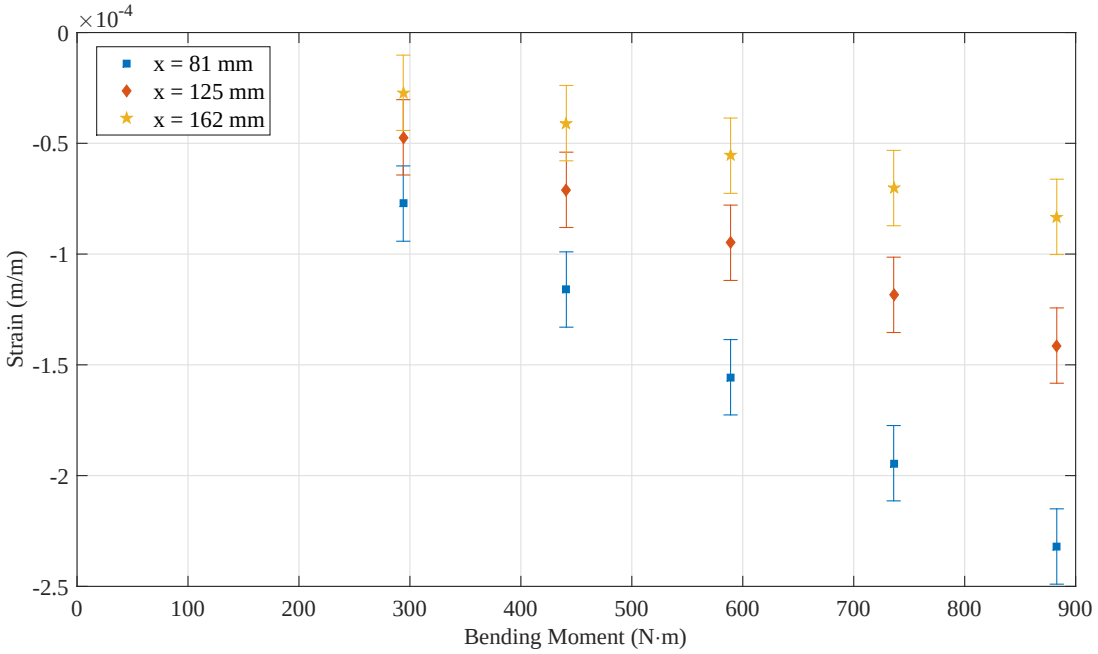


Figure 4.2: Strain versus load for 5 Spoke CRW under torsional load case with $\theta = 60°$

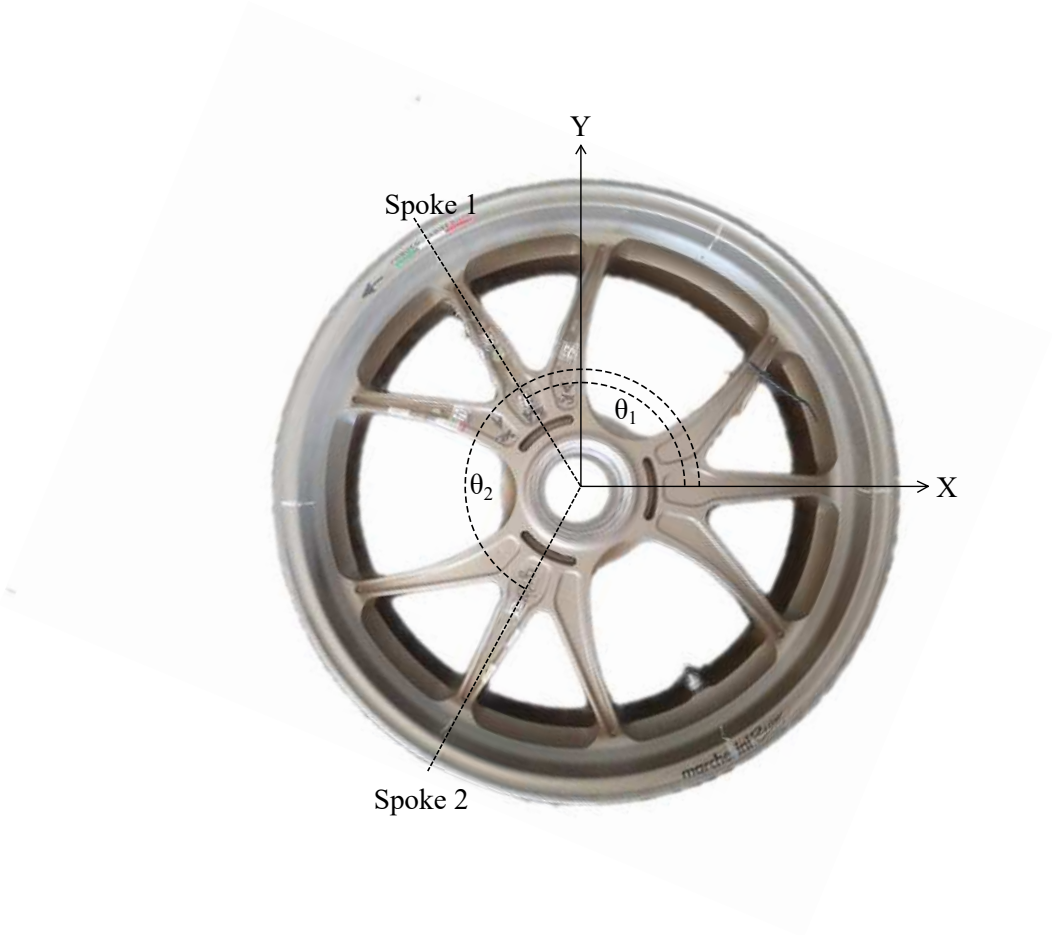


Figure 4.3: Relative orientations of primary and secondary spokes of 9 spoke ORW

The strain of the primary spoke and the modified strain of the secondary spoke in the same orientation were subtracted from one another. The average difference for each wheel was used as the uncertainty of the bending and torsional strain measurement. The uncertainty for the bending moment load case was $\pm 40\ \mu\frac{m}{m}$ and for the torsional load case it was $\pm 17\ \mu\frac{m}{m}$, as shown using error bars in Figure 4.1 and 4.2.

For wheels with the number of spokes not equal to a multiple of three, the strains were linearly interpolated to determine the strains on the secondary spoke at the same virtual orientation. This is valid because interpolation was preformed across a small angle, where there is a near linear change in strain.

4.3 Strain Distribution along Spoke Length

The strain versus the radial length along the spoke is shown in Figure 4.4 and Figure 4.5 for the bending and torsional load case, respectively. The three strain gauges placed on the wheel's spoke produced three data points that shows the general trend of the strain in each wheel sample. These were representative cases as the trend does not change with the spoke's orientation (θ). The hub and rim location for each wheel was indicated on each axes to give a sense of scale.

Additionally, the area moment of inertia about the local y- and z-axis of each wheel's spoke was overlaid on the strain plot for the bending and torsional load case, respectively. Five points were measured along the length of each wheel's spoke to give the trend in the area moment of inertia.

The area moment of inertia about the local y-axis was plotted on the same axes for the bending load case. When the wheel experiences the bending load case, the spokes at $\theta = 0^{\circ}$ and $\theta = 180^{\circ}$ experience a local bending moment around the local y-axis.

Similarly in the torsional load case, the spokes experience a local bending moment. However the direction of the local bending moment is about the local z-axes. Thus, the spoke's area moment of inertia around the local z-direction has the largest effect.

The strain for each wheel decreases in magnitude as the radial coordinate increases towards the outer rim. This trend was repeated for every orientation on every wheel sample. The spoke acts similar to a cantilever beam fixed at the hub with a bending moment and lateral force acting on the free end located at the rim. The strain can be calculated using the flexure formula (with Hooke's Law substituted), $\epsilon = Mc/IE$. As the internal bending moment decreases along the spoke's length so does the strain in the spoke, in spite of the decrease

in the moment of area. According to the flexure formula, the decrease in the area moment of inertia (I) causes an increase in strain. Thus, the internal bending moment seen within the spoke must decrease at a faster rate than the area moment of inertia. Thus, causing an overall decrease in strain along the length of the spoke.

With respect to the 9 spoke ORW, Figures 4.4(a) and Figure 4.5(a), the bending load case has a non-linear change in strain while the torsional load case follows a linear change in strain. This follows the trend seen in the area moment of inertia of both load cases. The area moment of inertia about the y-axis changes non-linearly, while the area moment of inertia is more linear about the z-axis.

The rate of decrease of the strain in each spoke is shown in Table 4.1. The 5 spoke CRW has a significantly lower gradient and magnitude of strain in both load cases than the other wheels. This wheel is an older design and not as optimized as the modern race wheels.

All the wheels use a tapering spoke which uses material more efficiently and lowering the overall weight of the wheel. The 9 spoke ORW and 7 spoke FW have a higher degree of taper, resulting in a higher strain gradient.

The strain gradients in the torsional load case were substantially lower than the bending load case. This is caused by the lower amount of tapering in this direction of the spoke. A more efficient wheel design is possible by further increasing the taper about the z-axis.

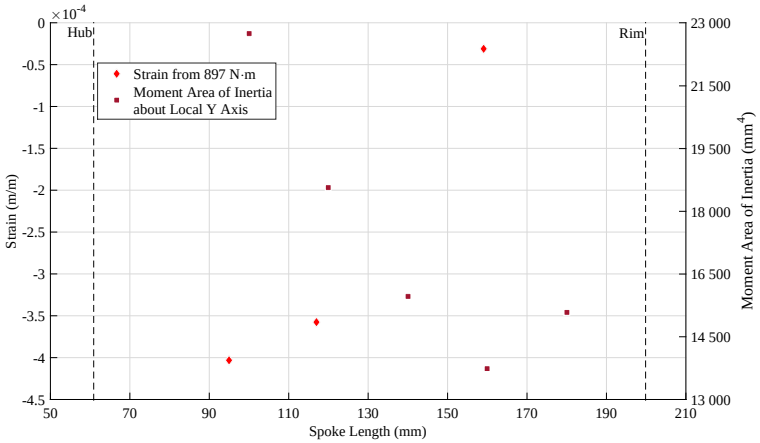
Table 4.1: Gradient of the strain along the length of the spoke

Wheel	Bending Load Case	torsional Load Case
9 Spoke ORW	-0.00581	-0.00520
5 Spoke CRW	-0.00181	-0.00067
7 Spoke FW	-0.00551	-0.00411

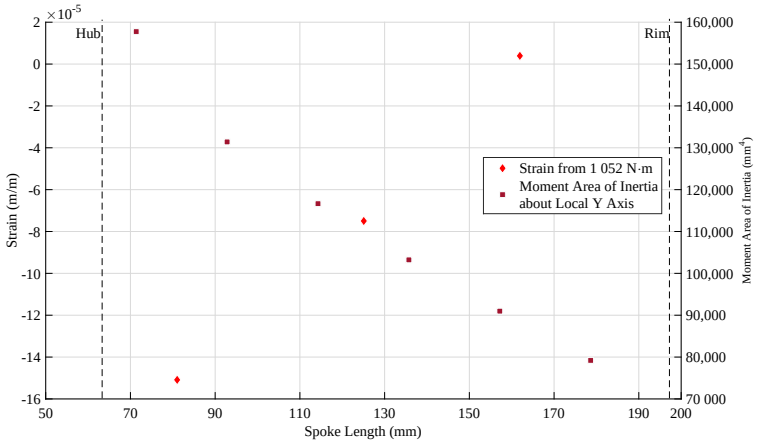
4.4 Strain Distribution with Orientation

As the wheel rotates relative to the load direction, the magnitudes of the internal, axial torsion and bending moment load in each spoke changes. Thus, there is a change in the strain as the spoke's orientation (θ) changes, as seen in Figure 4.6 and Figure 4.7 while under bending and torsional load, respectively.

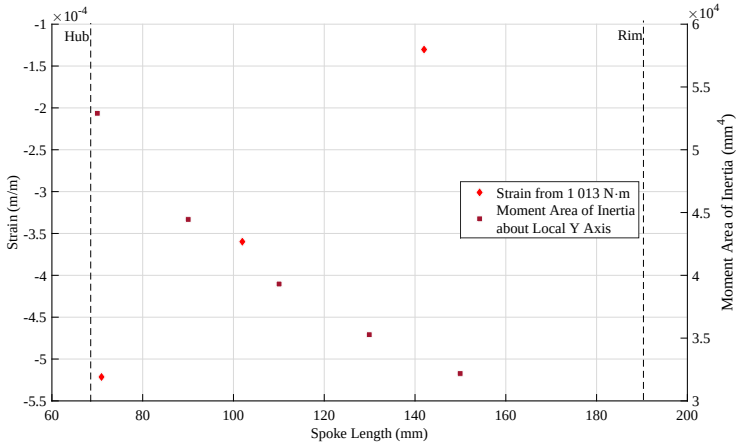
In both load cases, the strain follows a similar sinusoidal trend. The scale of the figures are such that the uncertainty bars (see Section 4.2) lie on top of the points and were thus removed from these figures.



(a) 9 Spoke ORW under bending load of 897 $N \cdot m$ at $\theta = 120°$

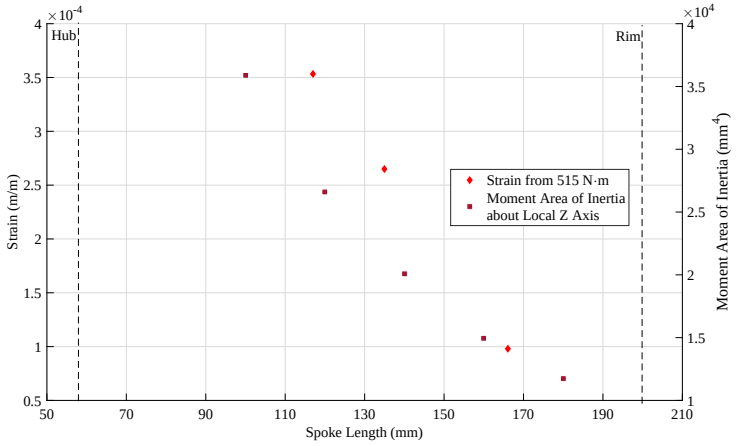


(b) 5 Spoke CRW under bending load of 1 052 $N \cdot m$ at $\theta = 105°$

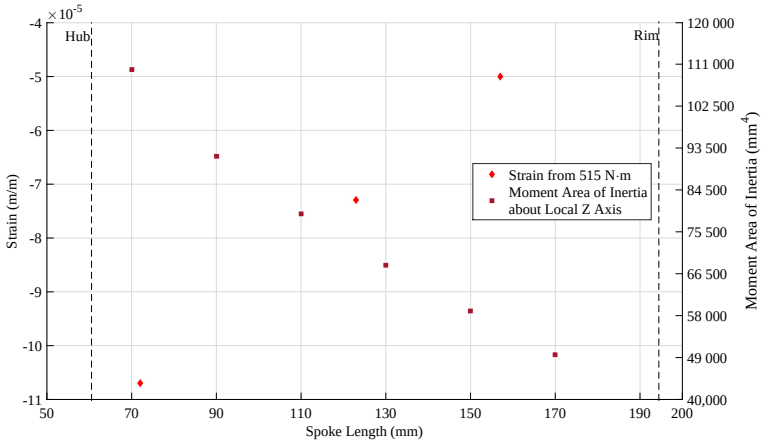


(c) 7 Spoke FW under bending load of 1 037 $N \cdot m$ at $\theta = 138°$

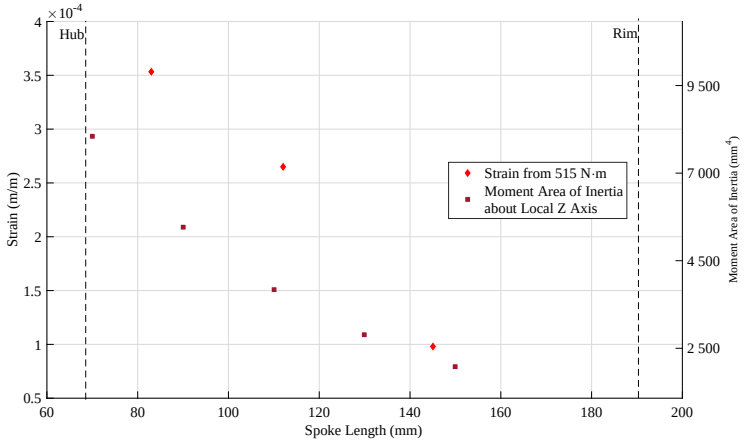
Figure 4.4: Strain versus radial position on the spoke for
(a) 9 Spoke ORW under bending load of 897 $N \cdot m$ at $\theta = 120°$
(b) 5 Spoke CRW under bending load of 1 052 $N \cdot m$ at $\theta = 105°$
(c) 7 Spoke FW under bending load of 1 037 $N \cdot m$ at $\theta = 138°$



(a) 9 Spoke ORW under torsional load of 515 $N \cdot m$ at $\theta = 171°$



(b) 5 Spoke CRW under torsional load of 515 $N \cdot m$ at $\theta = 165°$



(c) 7 Spoke FW under torsional load of 515 $N \cdot m$ at $\theta = 180°$

Figure 4.5: Strain versus radial position on the spoke for
(a) 9 Spoke ORW under torsional load of 515 $N \cdot m$ at $\theta = 171°$
(b) 5 Spoke CRW under torsional load of 515 $N \cdot m$ at $\theta = 165°$
(c) 7 Spoke FW under torsional load of 515 $N \cdot m$ at $\theta = 180°$

The strain has a maximum at $\theta \approx 0°$, a minimum at $\theta \approx 180°$. The measured strain was approximately fully reversing, i.e. $\|\sigma_{max}\| \approx \|\sigma_{min}\|$ for the bending load case. Hence, while a wheel is operating under normal use, during a cornering maneuver, the spoke experiences a small midrange stress component and a high alternating stress component.

In the bending load case, the moment exerted on the wheel caused the inner hub to rotate about the global y-axis. A large bending moment was generated around the spoke's local y-axis in the spokes that were orientated at $\theta = 0°$ or $\theta = 180°$. This in turn produced a component of the strain measured in the spoke.

Additionally, the inner hub shifted in the direction of the force. This was due to the axial force component of the loading applied to the wheel. Hence, a proportion of the normal strain in this orientation is due to the axial loading.

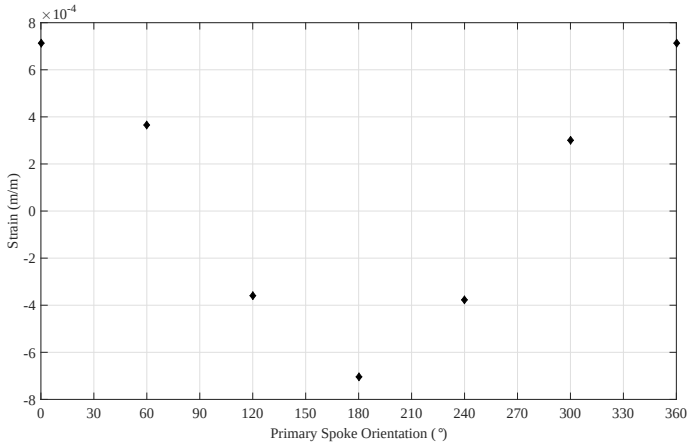
The spokes orientated at $\theta = 0°$ or $\theta = 180°$ act as a cantilever beam with a bending moment acting on its free end. The beam's deflection is dependent on the flexural rigidity (EI). Hence, the stiffness of the spoke, and ultimately the wheel, in this load case is governed by the area moment of inertia about the spoke's local y-axis.

In the bending load case, the spokes orientated at $\theta = 90°$ or $\theta = 270°$ do not experience a bending moment. The spokes in this orientation experience a torsion along their length caused by the twisting of the inner hub. the torsional deflection of the beam is governed by the angle of twist formula ($\phi = TL/GJ$). The formula is strongly dependent on the polar moment of inertia (J).

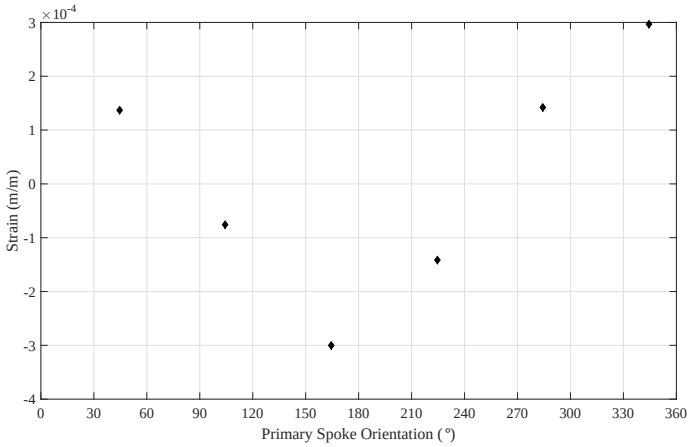
In the torsional load case, the spokes experience either a tensile or compressive strain, that varies slightly with the angle α or the wheel's orientation. The strain was not fully reversing as in the bending load case. The magnitude of the strain was much smaller in this load case. In particular, the 5 spoke CRW has an amplitude that was similar to the uncertainty calculated in Section 4.2, i.e 60 $\mu m/m$ compared to an uncertainty of 17 $\mu m/m$.

If a pure couple moment was applied then the strain would be constant or independent of the angle or the wheel's orientation; both the load and the wheel are axisymmetric. However, the test rig applies both a radial load and a torsional moment, that causes the strain on the spoke to vary with orientation. The sinusoidal variation was measured to have a maximum near 90° and a minimum near 270° for all three wheel types.

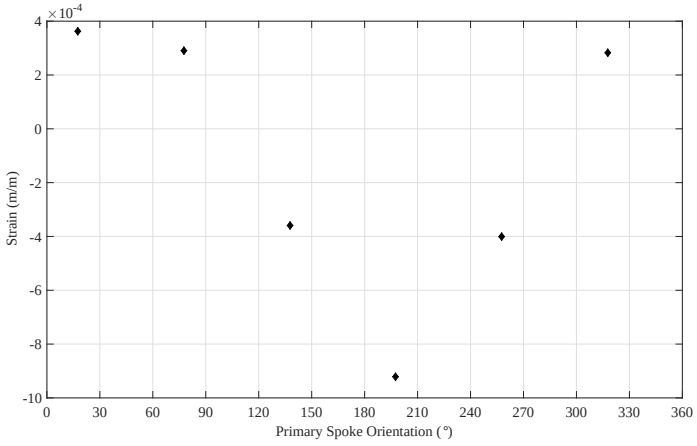
In this load case, the inner hub rotates about the the global z-axis (rolling axis) and shifts laterally in the direction of the force (along the global x-axis). The inner hub's rotation causes a large bending about the local z-axis on each spoke, independent of the spoke's orientation. The spoke's stiffness is dependent on the area moment of inertia about the local z-axis.



(a) 9 Spoke ORW under bending load of 897 $N \cdot m$ at $x = 117\ mm$



(b) 5 Spoke CRW under bending load of 1 052 $N \cdot m$ at $x = 125\ mm$



(c) 7 Spoke FW under bending load of 1 100 $N \cdot m$ at $x = 102\ mm$

Figure 4.6: Strain versus spoke orientation (θ) for
(a) 9 Spoke ORW under bending load of 897 $N \cdot m$ at $x = 117\ mm$
(b) 5 Spoke CRW under bending load of 1 052 $N \cdot m$ at $x = 125\ mm$
(c) 7 Spoke FW under bending load of 1 100 $N \cdot m$ at $x = 102\ mm$

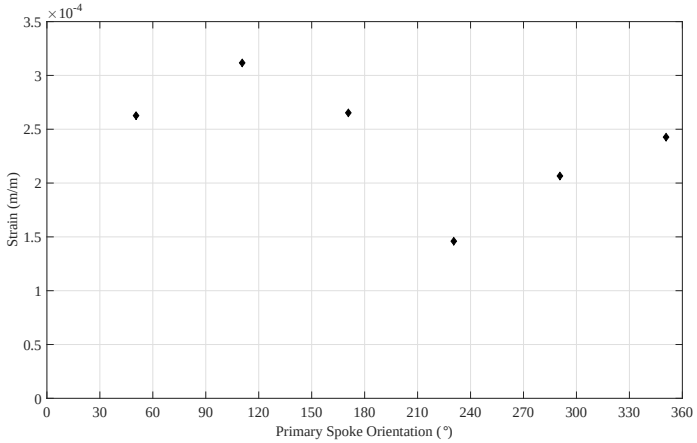
The lateral shift of the inner hub caused an axial strain (compression or tension) within the spoke at $\theta = 0°$ and $\theta = 180°$ and a large bending strain at $\theta = 90°$ and $\theta = 270°$. This caused the change in the strain with orientation.

A high axial stiffness on a spoke creates a smaller change as the spoke changes orientation. The 5 spoke CRW has a much larger cross sectional area and was made from an aluminium alloy with a high Young's modulus (compared to magnesium for the 9 spoke ORW and 7 spoke FW). Hence, the change of strain with orientation in the 5 spoke CRW was much lower than the other wheels.

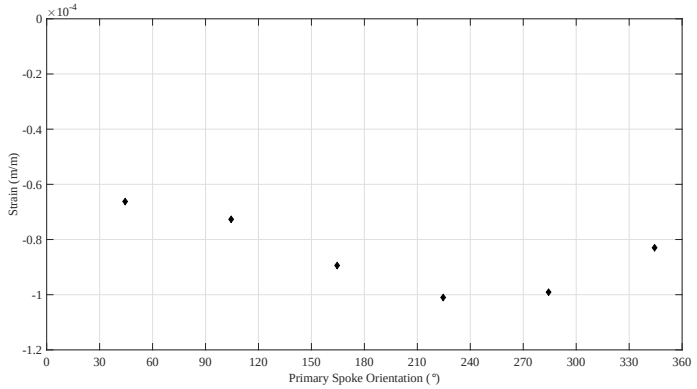
The fully reversing nature of the bending load case is more critical than the torsional load case. The fully reversing strain creates a larger amount of fatigue damage according to the ASME fatigue failure theory[14].

Furthermore, the bending load case caused a higher magnitude of strain in each wheel as compared to the torsional load case. On average across all the tested wheels, the bending load case was 65 % higher than the torsional load case for the given load rating of each wheel.

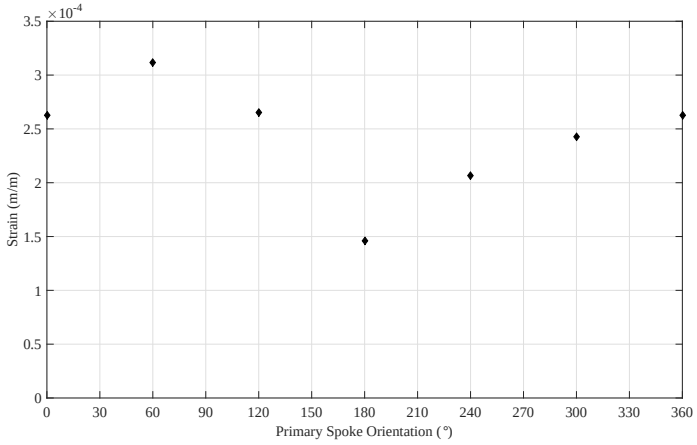
The torsion applied to each wheel was 515 $N \cdot m$ compared to the average bending moment which was 1 016 $N \cdot m$. For a better understanding, the maximum strain experienced by each wheel was normalised by the load. This showed that the wheels experienced on average 32 % more strain per a unit load in the bending load case compared to the torsional load case.



(a) 9 Spoke ORW under torsional load of 515 $N \cdot m$ at $x = 80\ mm$



(b) 5 Spoke CRW under torsional load of 515 $N \cdot m$ at $x = 123\ mm$



(c) 7 Spoke FW under torsional load of 515 $N \cdot m$ at $x = 100\ mm$

Figure 4.7: Strain versus spoke orientation (θ) for
(a) 9 Spoke ORW under torsional load of 515 $N \cdot m$ at $x = 80\ mm$
(b) 5 Spoke CRW under torsional load of 515 $N \cdot m$ at $x = 123\ mm$
(c) 7 Spoke FW under torsional load of 515 $N \cdot m$ at $x = 100\ mm$

5 Finite Element Analysis

Finite element analyses (FEA) of the wheels experiencing a bending moment and a torsional load were conducted. The simulations predicted the maximum normal strain at the location of each strain gauge, and provided further confidence in the strain measurements.

5.1 Finite Element Modelling Details

The models were created with SolidWorks Premium 2016 (with SP04). The wheel profile specified by ETRTO [15] was used, with the required dimensions for the *drop-centre rims with* 5° *tapered bead seats*. The spoke geometry was measured using inside/outside callipers or directly using a vernier calliper. The uncertainty of the vernier calliper was $\pm 0.05\ mm$. Additional uncertainty was created through the use of callipers and go/no-go gauges to measure fillets.

The wheel simulations were preformed using the commercial software, Ansys 15.0. The Ansys static structural component block was used, with the geometry imported in parasolid format. Aluminium, magnesium and steel were used; their material properties as shown in Table 5.1. The strain at the gauge locations, mesh quality and deformation of the wheel were exported to Microsoft Excel and MATLAB for comparison with the experimental results.

Table 5.1: Material properties for FEA

Material	Density (kg/m^3)	Young's Modulus (GPa)	Poisson's Ratio
Steel	7 850	200	0.30
Aluminum	2 770	71	0.33
Magnesium	1 800	45	0.35

5.2 Investigation of Mesh Independence

The mesh independence was investigated using the bending load case. The boundary conditions were kept constant, and the type of mesh and element size varied. The wheel was fixed on the outer lip and a remote force acted through the mounting face of the wheel. Only a single spoke of the wheel was modelled (without symmetry conditions) to reduce the computation time, as shown in Figure 5.1.

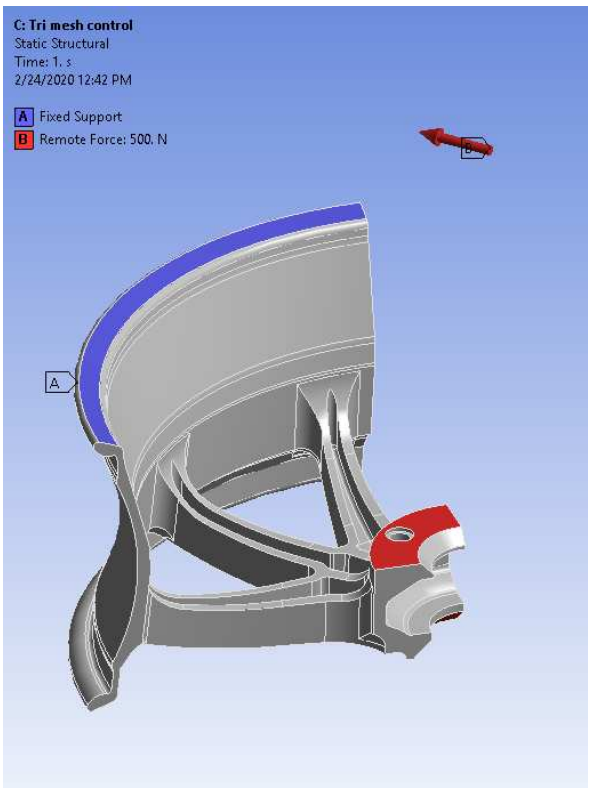


Figure 5.1: Geometry used in mesh independence study

Quadrahedrals and tetrahedron elements were evaluated. The quadrilateral elements produced a low element quality because of the complex geometry of the wheel. The Ansys Mesher could not generate a mesh with element sizes smaller than 2 mm or larger than 4 mm, with either type of element.

The results of using the two different element type can be seen in Figure 5.2. The element quality tended to a value of 82.5% using the tetrahedron elements, while the element quality tended to 72% using quadrilateral elements.

Strain was of primary interest, thus it was used to determine the convergence of the mesh. The number of elements was controlled by manipulating the element size. The element size started at 5 mm and was decreased by 1 mm and the percent change of the results recorded. The strain results are plotted on the left axis against the number of elements as seen in

Figure 5.2, and the average *element quality* of the mesh is shown on the right axis. Ansys's *element quality* assigns a numerical value to each element of the mesh that is dependent on the node-point distribution, smoothness and skewness of the element.

Using tetrahedral elements, the maximum principal strain tended to a value of 825.7 $\mu\frac{m}{m}$ as the number of elements is increased. When using quadrilateral elements, the maximum principal strain tended to a value of 826.1 $\mu\frac{m}{m}$. This is 0.05% difference between the two element types when using a large amount of elements.

The best number of elements should result in low computational time, while not sacrificing the accuracy of the simulation results. Reducing the element size from 3 to 2 mm, the number of elements increases nearly 70 %, with the mesh quality increasing by 1.4 % to 83.7 %. The increase in the number of elements significantly increased the computational time while the strain changed by 0.1 %. The change in the results did not warrant the increase in the computational time.

The best mesh for this study was found to be tetrahedral elements, with an element size of 3 mm. This would result in a mesh quality of over 80 %, while the computational time would be kept acceptable.

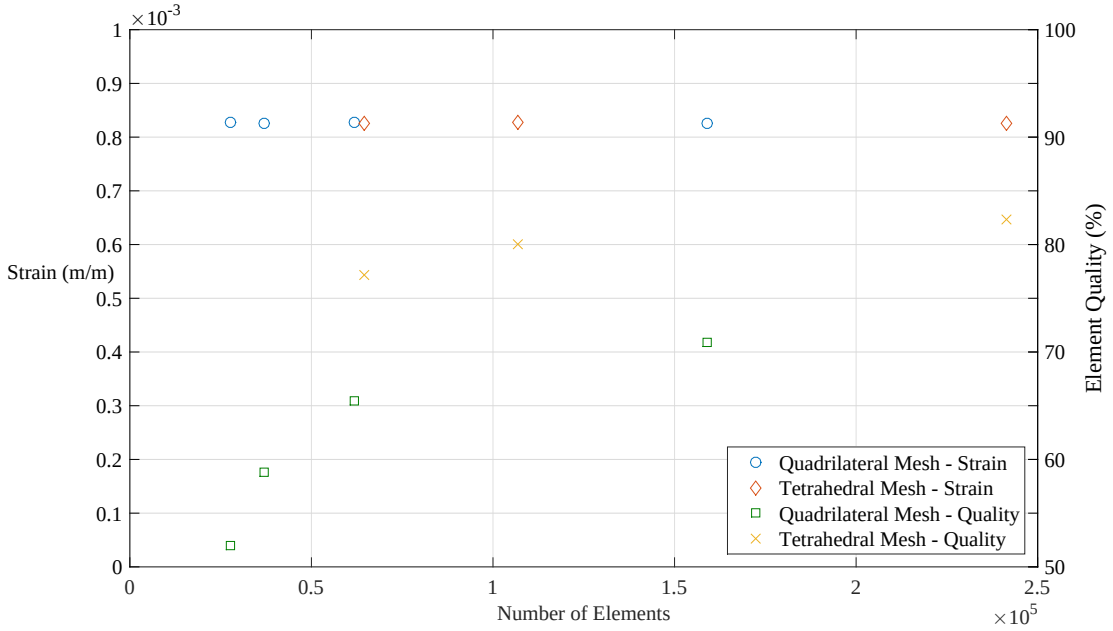


Figure 5.2: Strain and element quality versus number of elements

5.3 Investigation of Boundary Conditions

The boundary conditions of a simulation refer to the supports, connections between bodies and the forces placed on the elements. These have a large effect on the results of the simulation. Multiple simulations were preformed with differing boundary conditions and the results were compared to the experimental data to determine the most accurate boundary conditions.

Three combinations of boundary conditions were simulated. These varied in complexity but used the same mesh, as defined in Section 5.2. The boundary conditions were investigated using the 9 spoke ORW, because of the complexity of the spokes.

The first or simplified boundary conditions used a remote force placed on the hub and cone washer face as seen in Figure 5.3. There were no additional bodies that required contact properties to be defined. The force was offset 406 mm away from the hub face in the z-direction, which simulated the load arm. The magnitude of the force was $F_y = 2845.6\ N$ and $F_z = -750.8\ N$, as experienced in the experiment. A fixed support (that allows no movement of the nodes) was placed on the outer rim face; simulated being clamped to a plate, as in the experiment.

The second and third boundary conditions both used the geometry of the full test rig (including the load arm) to provide a more accurate simulation of the introduction of the force applied to the wheel. The force, of the same magnitude as in the first boundary condition case, was placed on the end of the load arm which was at the same distance as the first simulation, as seen in Figure 5.4. The fixed support on the clamped face of the wheel was the same as the first simulation.

The contacts between the various components significantly alter the results of the simulation. In the Ansys environment, there are five possible contact conditions as described below [16]:

Bonded Linear contact that allows no sliding or separation.

No separation Linear contact that does not allow separation.

Frictionless Non-linear contact that allows bodies to separate and slide (with a friction coefficient of zero).

Rough Non-linear contact that allows bodies to separate but not slide (with an infinite friction coefficient).

Frictional Non-linear contact that allows bodies to separate and slide (with an user defined friction coefficient).

A contact is linear or non-linear if the contact's stiffness matrix changes with the solution. Thus, an iterative solver is used that should produce a converging solution (divergence is possible in a non-linear solution). Furthermore, a non-linear contact may take longer to solve than a linear solution and may not be necessary if the contacts are suitably defined with linear contacts.

The second simulation used linear contacts, while the third used non-linear contacts, as seen in Table 5.2 and Figure 5.4. The linear simulation reduced computing time and any possibility of solution divergence because multiple iterations were not needed.

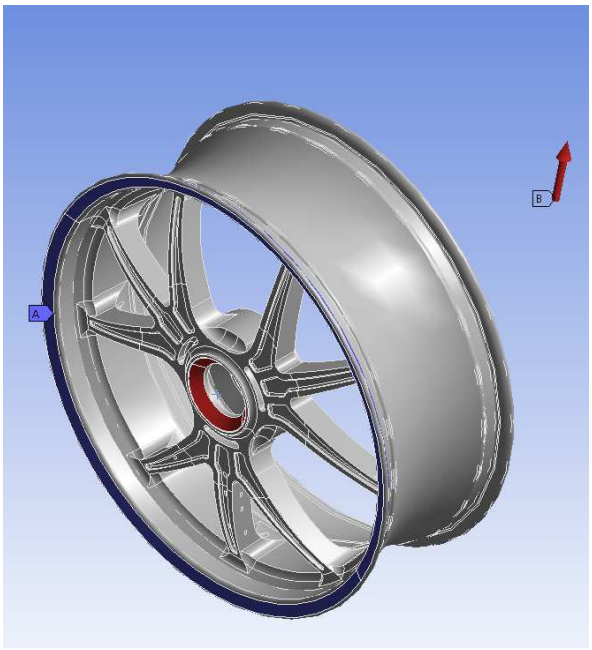


Figure 5.3: Simplified boundary conditions

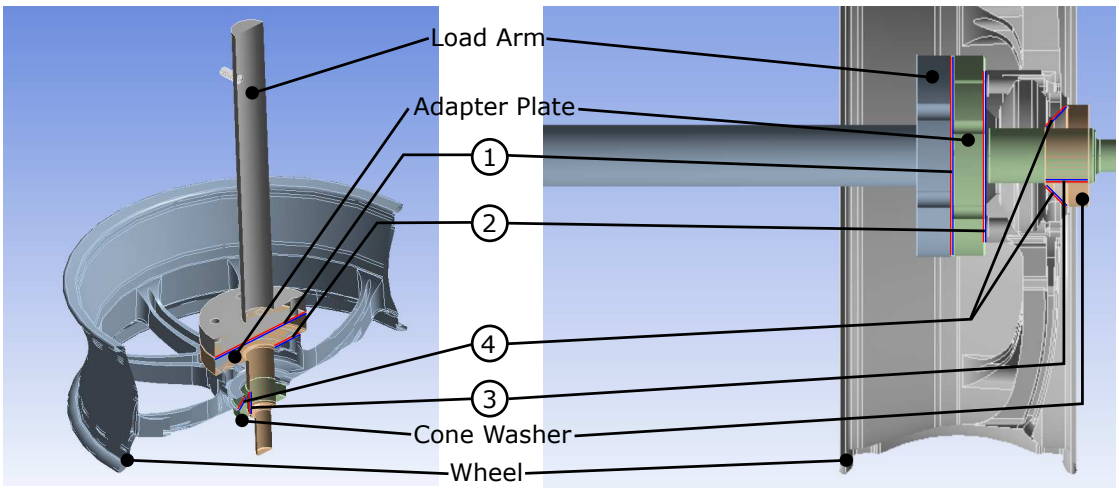


Figure 5.4: Full test rig simulation with connections

Table 5.2: Contacts in linear and non-linear simulation

Contact No.	Body 1	Body 2	Non-Linear Sim.	Linear Sim.
1	Load Arm	Adapter Plate	Frictionless	Bonded
2	Adapter Plate	Wheel	Frictionless	No-Separation
3	Adapter Plate	Cone Washer	Bonded	Bonded
4	Cone Washer	Wheel	Frictionless	Bonded

Both the linear and non-linear simulation used rigid beam elements to simulate bolts between the load arm and the adapter (Connection 2). In the linear simulation, these elements prevented sliding between these components and the no-separation contact prevented separation. In the non-linear simulation, these elements prevented sliding and separation between these components, while the frictionless support connected the components.

In the experiment the cone washer was held on the adapter plate by a nut that was torqued to 230 $N \cdot m$. This was simulated by a bonded connection (Connection No. 3) in both simulations. The high pre-load on the nut did not allow sliding or separation between the cone washer and adapter plate.

The pre-load on the nut also holds the cone washer in firm contact with the wheel, but the wheel may move away from the cone washer if the deformation is great enough. Thus, in the non-linear simulation this contact (Connection No. 4) was set to frictionless, while the linear simulation did not allow for separation.

Table 5.3 compares the normal strain in the direction of the primary spoke (when $\theta = 0°$) when the wheel was loaded to 1195 $N \cdot m$. There was little difference between each boundary condition set, however the linear boundary conditions were the most accurate as compared to the experimental results and solved the quickest. This set-up was used for each simulation.

Table 5.3: Boundary condition comparison

	Strain ($\mu m/m$)	Percentage Difference
Experiment	0.6458	
Boundary Set 1 (Remote Force)	618.6	-4.40 %
Boundary Set 2 (Non-Linear)	635.2	-1.68 %
Boundary Set 3 (Linear)	645.9	+0.01 %

5.4 Simulation Results

A finite element analysis was performed on each wheel with the mesh controls and boundary conditions described in Sections 5.2 and 5.3, respectively. The normal stress in the direction of the spoke is plotted versus the wheel orientation (θ) in Figure 5.5 and Figure 5.6 for the bending and torsional load case, respectively.

The FEA was preformed with 4° increments in spoke orientation, which leads to 90 simulations preformed over a full rotation of the wheel. This provided a nearly continuous line as seen in the Figures 5.5 and 5.6.

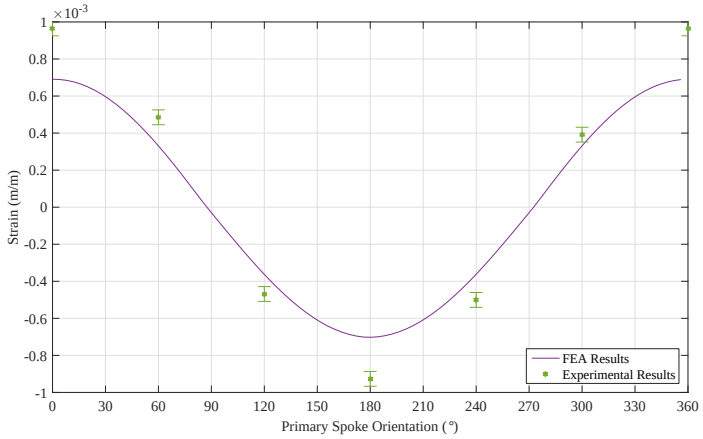
The maximum normal strain at the centre strain gauge location on the spoke was compared to the experimental strain gauge at the same position. The strain was measured in the direction of the strain gauge by adding a coordinate system that followed the strain gauge. The uncertainty values shown are $\pm 40\ \mu\frac{m}{m}$ for the bending load case and $\pm 17\ \mu\frac{m}{m}$ for the torsional load case, as calculated in Section 4.2.

In the bending load case, the FEA was symmetric about the x-axis with a sinusoidal variation that was similar to the experimental results. The maximum strain in all the wheels were predicted to be slightly lower in magnitude than the experimental results. The maximum strain is of primary interest, as the value dictates the fatigue crack growth and ultimately the wheel failure. The FEA simulation predicted the strain to be 21% lower at these peak orientations. At orientations between the peaks the difference between the experimental and simulation results drops to below 9% for all the wheels.

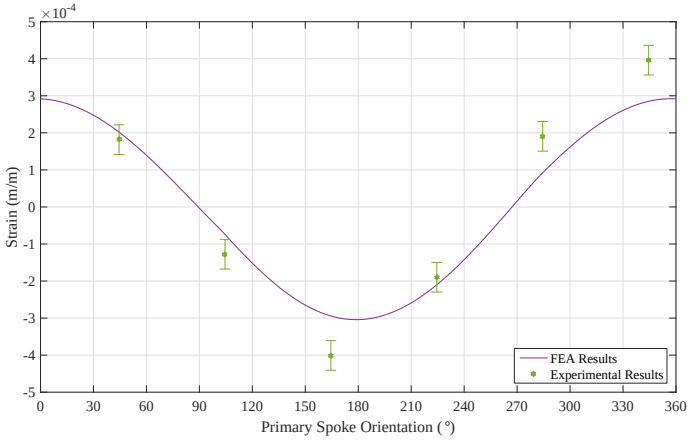
The maximum strain for all the wheels occurs near the 0° orientation, with the minimum occurs at 180°. The orientation of the maximum strain for the 7 spoke FW experimental strain was shifted 15° to the right. This is due to the curved nature of the spokes on this wheel.

For the torsional load case the difference between the simulation and experimental results is 14%. In the case of the 9 spoke ORW the simulation under-predicts the strain. In the case of the 7 spoke FW the simulation over-predicts the strain.

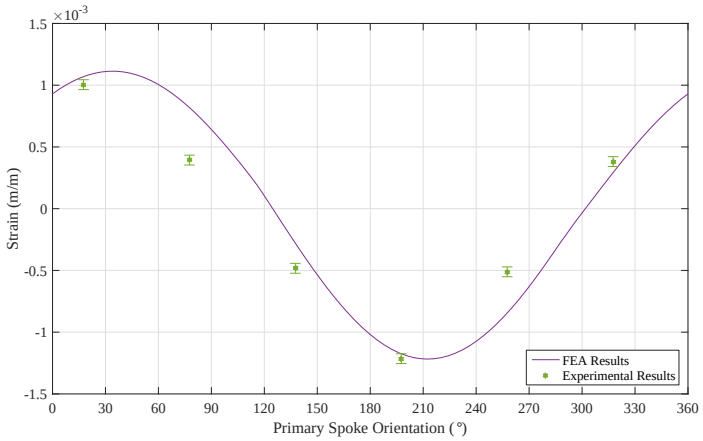
The 5 spoke CRW was the most accurately simulated across both load cases. This is due to the simple geometry of the spokes. The other wheels have more complex geometry that may not be accurately represented in the CAD. Considering that the wheel geometries needed to be measured by hand using calipers, the experimental and simulation results show good agreement.



(a) 9 Spoke ORW under bending load of 1 195 $N \cdot m$ at $x = 117\ mm$



(b) 5 Spoke CRW under bending load of 1 402 $N \cdot m$ at $x = 125\ mm$



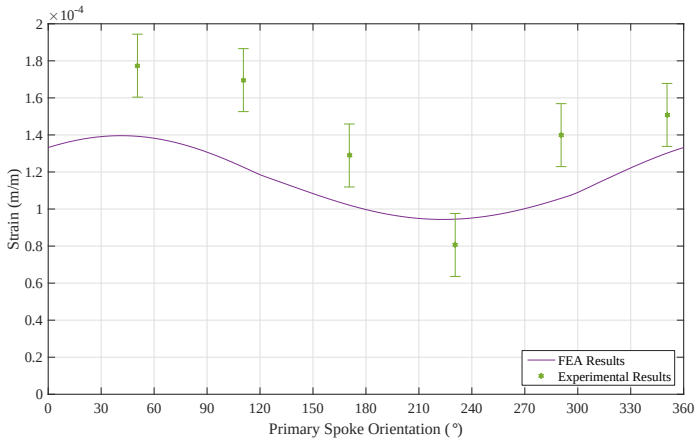
(c) 7 Spoke FW under bending load of 1 340 $N \cdot m$ at $x = 102\ mm$

Figure 5.5: Finite element strain and experimentally-measured strain versus spoke orientation (θ) for

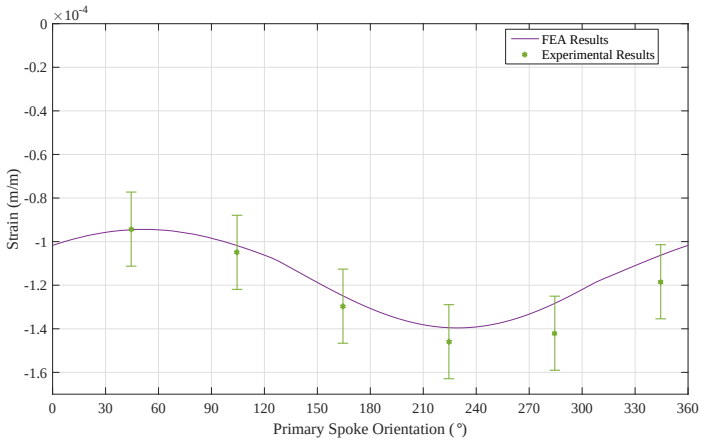
(a) 9 Spoke ORW under bending load of 1 195 $N \cdot m$ at $x = 117\ mm$

(b) 5 Spoke CRW under bending load of 1 402 $N \cdot m$ at $x = 125\ mm$

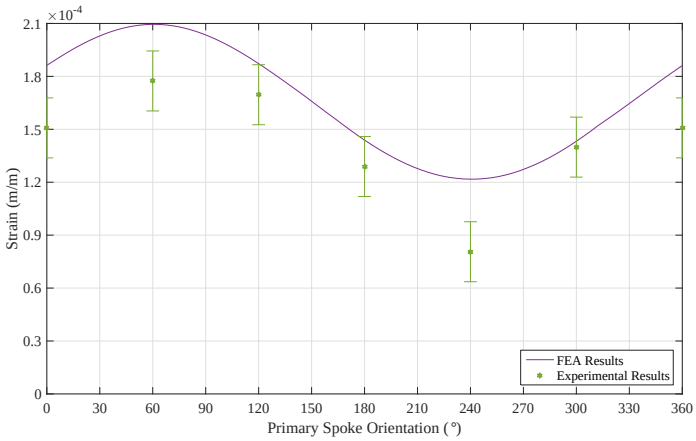
(c) 7 Spoke FW under bending load of 1 340 $N \cdot m$ at $x = 102\ mm$



(a) 9 Spoke ORW under torsional load of 736 $N \cdot m$ at $x = 80\ mm$



(b) 5 Spoke CRW under torsional load of 736 $N \cdot m$ at $x = 123\ mm$



(c) 7 Spoke FW under torsional load of 736 $N \cdot m$ at $x = 100\ mm$

Figure 5.6: Finite element strain and experimentally-measured strain versus spoke orientation (θ) for

(a) 9 Spoke ORW under torsional load of 736 $N \cdot m$ at $x = 80\ mm$

(b) 5 Spoke CRW under torsional load of 736 $N \cdot m$ at $x = 123\ mm$

(c) 7 Spoke FW under torsional load of 736 $N \cdot m$ at $x = 100\ mm$

6 Simplified Model

A simplified model of the solid mechanics of a wheel with an applied load at the hub centre was developed to provide insights into the effect of different loadcases for a large variety of wheel geometries. The underlying principle of the model uses finite elements to represent the geometry of the wheel. This formulation is a shear-undeformable model, which holds the plane cross-sections perpendicular to the longitudinal centroid axis.

The flowchart of the program is shown seen in Figure 6.1. Each block was a separate module that will be explained in the sections below. The MATLAB code was developed using the methods from [17] and [18].

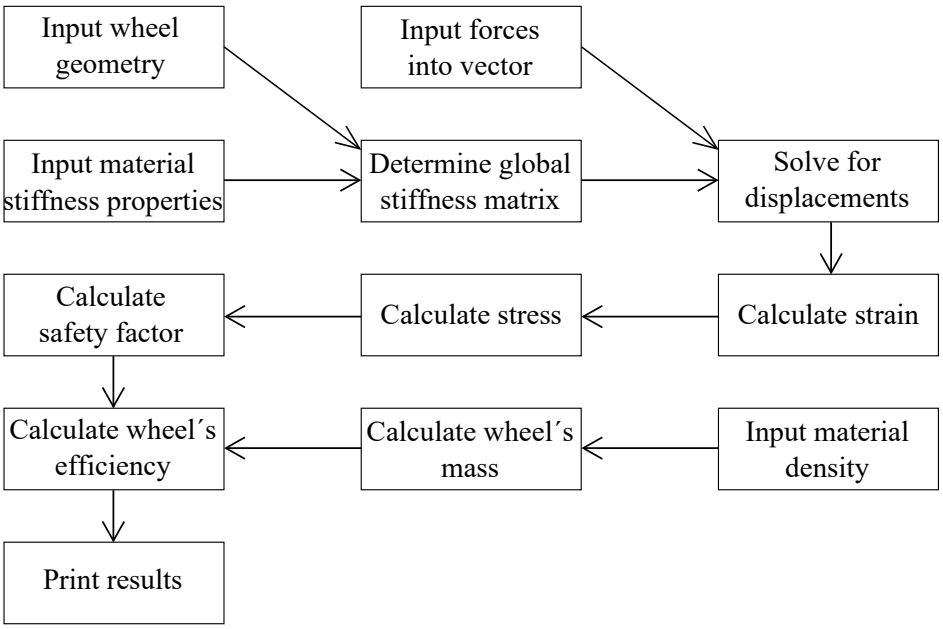


Figure 6.1: Simplified model data flow

6.1 Required Inputs

The required inputs for the simplified model analysis are the node geometry, boundary conditions, spoke and material properties. The analysis inputs are the type of wheel and the orientation of the primary spoke. Using this information, the wheel inputs function calculates the nodes coordinates in the global coordinate system and returns a MATLAB structure element containing the preset wheel data.

Two co-ordinate systems are defined as shown in Figure 6.2. The global coordinate system $[X, Y, Z]$ has its origin located at the centroid of the wheel in the X-Y plane, with the Z-axis is the rolling axis of the wheel and in the direction that forms a right-hand coordinate system. Each spoke has its own local coordinate system $[x_n, y_n, z_n$ where $n \in 1 \ldots N]$, with the x-axis aligned with the spoke directed away the wheel's centre. The local z-axis is parallel to the global Z-axis.

The node numbering convention was kept consistent between wheels. Numbering started at the outer rim, with the primary spoke inline with the positive X-axis. The outer rim nodes were numbered in a counter clockwise direction; the inner nodes were numbered, starting once again at the primary spoke.

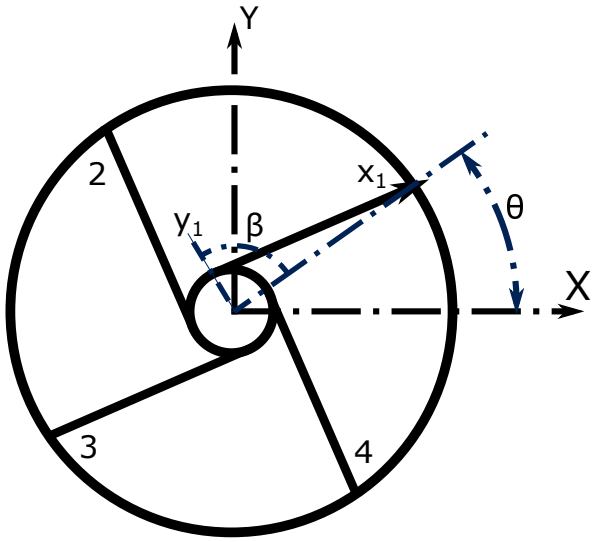


Figure 6.2: Simplified model coordinate system

The spoke orientation (θ) was measured from the global X-axis to a radial line passing through the spoke-to-outer-rim node of interest, which was consistent with the orientation used in the experimental results. The spoke angle (β) was a measure of the slant of the spoke; i.e. when $\beta = 0°$ the spoke is parallel to a radial line passing through the origin. The spoke angle is a geometric property of the wheel and does not change with the spoke's orientation.

The node's coordinates were calculated within the global coordinate system and were stored in a matrix named *NodeCoodinates*. The *Connection* matrix has a row for each element, in each row the nodes which that element connects to were stored.

The *FixedDof* matrix list the degrees of freedom (DoF) of each node that were fixed. Each node has 6 DoF and were numbered in the following order; node 1 with $F_{x,n}$, $F_{y,n}$, $F_{z,n}$, $M_{x,n}$, $M_{y,n}$, $M_{z,n}$ until node n.

The material properties were set to those used in the FEA, as described in Section 5. The spoke geometry was measured from each computer model. The spoke cross-section at the centre strain gauge was used to calculate the area, polar moment of inertia and the area moment of inertia.

Material properties needed to define the material strength and calculate the required factors of safety are listed in Table 6.1. $ALSi11Mg$ is typically used for cast aluminium wheels, with properties were listed for 10^6 cycles. A typical alloy for forged magnesium wheels is $AZ31B$, with fatigue properties listed for 10^6 cycles as well.

Table 6.1: Strength properties of materials

Material	Yield Strength (MPa)	Endurance Strength (MPa)	Source
$AlSi11Mg$	165	80	[19]
$AZ31B$ Magnesium	163	118	[20], [21]

6.2 The Euler-Bernoulli Beam

A formulation for a three-dimensional Euler-Bernoulli beam element is described in this section. This is not a complete derivation, and only offers some background knowledge to better understand the coming sections. A complete derivation can be found in the literature [22], [23], [24]. A 3D element is shown in Figure 6.3, with lateral deformation (w) in the y direction, transverse deformation (v) in the z direction and longitudinal deformation (u) in the x direction.

Node 1 and 2 each have 6 degrees of freedom; 3 displacements and 3 rotations. The displacement vector for node n is given in Equation 6.1, and the displacement vector for the element in Equation 6.2.

$$\boldsymbol{u^{n,e}} = \begin{bmatrix} u & w & v & \theta_x & \theta_y & \theta_z \end{bmatrix} = \begin{bmatrix} u & w & v & \theta_x & \frac{dw}{dx} & \frac{dv}{dx} \end{bmatrix} \tag{6.1}$$

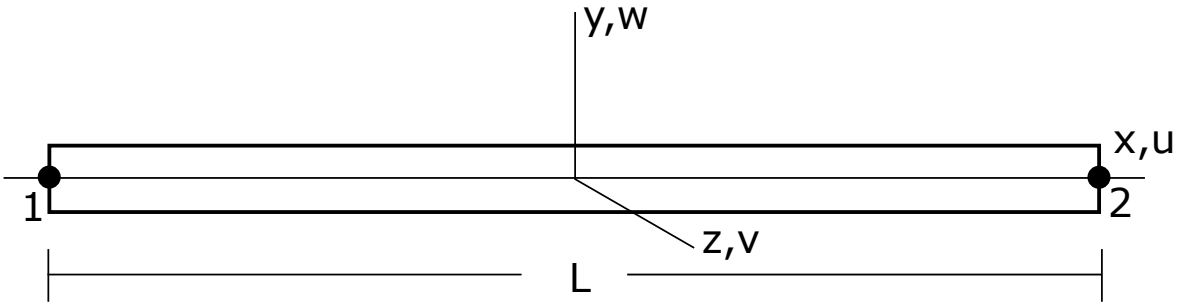


Figure 6.3: 3D Euler-Bernoulli beam element

$$\boldsymbol{u^e} = \begin{bmatrix} u^{1,e} & u^{2,e} \end{bmatrix} \tag{6.2}$$

The transverse and lateral displacement is interpolated between the nodal points using a cubic shape function. The displacement is calculated by multiplying the shape function matrix with element displacement vector, as shown in Equation 6.3. Using the Hermite shape functions, shown in Equation 6.4, the displacement at any point between the two nodes can be interpolated. The Hermite functions can be made more general by transforming from the local coordinate system to a natural coordinate system by letting $\zeta = 2x/L$, where $\zeta \in [-1, 1]$.

$$\boldsymbol{u(x)} = \begin{bmatrix} u(x) \\ w(x) \\ v(x) \end{bmatrix} = \boldsymbol{N u^e} \tag{6.3}$$

$$\boldsymbol{N} = \begin{bmatrix} N_1 & 0 & 0 & 0 & 0 & 0 & N_4 & 0 & 0 & 0 & 0 & 0 \\ 0 & N_2 & 0 & 0 & 0 & N_3 & 0 & N_5 & 0 & 0 & 0 & N_6 \\ 0 & 0 & N_2 & 0 & N_3 & 0 & 0 & 0 & N_5 & 0 & N_6 & 0 \end{bmatrix} \tag{6.4}$$

Where

$$\begin{aligned} N_1 &= 1 - \tfrac{x}{L} &&= \tfrac{1}{2}(1-\zeta) \\ N_2 &= 1 - \tfrac{3x^2}{L^2} + \tfrac{2x^3}{L^3} &&= \tfrac{1}{2}(1-\zeta)^2(2+\zeta) \\ N_3 &= x - \tfrac{2x^2}{L} + \tfrac{x^3}{L^2} &&= \tfrac{1}{2}(1-\zeta)^2(1+\zeta) \\ N_4 &= \tfrac{x}{L} &&= \tfrac{1}{2}(1+\zeta) \\ N_5 &= \tfrac{3x^2}{L^2} - \tfrac{2x_3}{L^3} &&= \tfrac{1}{2}(1+\zeta)^2(2-\zeta) \\ N_6 &= -\tfrac{x_2}{L} + \tfrac{x^3}{L^2} &&= \tfrac{1}{2}(1+\zeta)^2(\zeta-1) \end{aligned}$$

The strain energy of the element is derived from the basic energy formula, $U = \int F dx$, resulting in $U = 1/2 \int_V \sigma \epsilon dV$. This basic equation can be manipulated into the form of Equation 6.5, which can be made into a function of the element stiffness matrix, as shown in Equation 6.6 and the symmetric 12-by-12 matrix below. This provides the stiffness of single Euler-Bernoulli beam element within a local coordinate system.

An additional note should be made of the polar moment of inertia (J^*). This formulation assumes the beam has a circular cross-section. The polar moment of inertia is modified to an equivalent circular cross-section through standard formulas.

$$\begin{aligned} U_e &= \frac{1}{2}\int_{-L/2}^{L/2} EI\left(\frac{\partial^2 u}{\partial x^2}\right)^2 \, dx \\ &= \frac{1}{2}\int_{-1}^{1} \frac{EI}{L^4/16}\left(\frac{\partial^2 u}{\partial \zeta^2}\right)^2 \frac{L}{2} \, d\zeta \\ &= \frac{1}{2}\boldsymbol{u}^{e,T}\frac{8EI}{L^3}\int_{-1}^{1} \boldsymbol{N}''^T\boldsymbol{N}'' d\zeta \boldsymbol{u}^e \\ &= \frac{1}{2}\boldsymbol{u}^{e,T}\boldsymbol{K}^e\boldsymbol{u}^e \end{aligned} \tag{6.5}$$

Where

U_e	=	Strain energy of element
L	=	Element length
E	=	Young's modulus
I	=	Area moment of inertia
$\boldsymbol{N}''$	=	$\frac{\partial^2 \boldsymbol{N}}{\partial \zeta^2}$

$$\boldsymbol{K}^e = \frac{8EI}{L^3}\int_{-1}^{1} \boldsymbol{N}''^T\boldsymbol{N}'' d\zeta \tag{6.6}$$

$$\boldsymbol{K}^e = \begin{bmatrix} \frac{EA}{L} & 0 & 0 & 0 & 0 & 0 & -\frac{EA}{L} & 0 & 0 & 0 & 0 & 0 \\ & \frac{12EI_Z}{L^3} & 0 & 0 & 0 & \frac{6EI_Z}{L^2} & 0 & -\frac{12EI_Z}{L^3} & 0 & 0 & 0 & \frac{6EI_Z}{L^2} \\ & & \frac{12EI_Y}{L^3} & 0 & -\frac{6EI_Y}{L^2} & 0 & 0 & 0 & -\frac{12EI_Y}{L^3} & 0 & -\frac{6EI_Y}{L^2} & 0 \\ & & & \frac{GJ^*}{L} & 0 & 0 & 0 & 0 & 0 & -\frac{GJ^*}{L} & 0 & 0 \\ & & & & \frac{4EI_Y}{L} & 0 & 0 & 0 & \frac{6EI_Y}{L^2} & 0 & \frac{2EI_Y}{L} & 0 \\ & & & & & \frac{4I_Z}{L} & 0 & -\frac{6EI_Z}{L^2} & 0 & 0 & 0 & \frac{2EI_Z}{L} \\ & & & & & & \frac{EA}{L} & 0 & 0 & 0 & 0 & 0 \\ & & & & & & & \frac{12EI_Z}{L} & 0 & 0 & 0 & -\frac{6EI_Z}{L^2} \\ & & & & & & & & \frac{EI_Z}{L^3} & 0 & \frac{6EI_Y}{L^2} & 0 \\ & & & & & & & & & \frac{GJ^*}{L} & 0 & 0 \\ & & & & & & & & & & \frac{4EI_Y}{L} & 0 \\ & & & & & & & & & & & \frac{4EI_Z}{L} \end{bmatrix} \tag{6.7}$$

6.3 Global Stiffness Matrix

The Global Stiffness Matrix function returns the global stiffness matrix for a particular structure. The function calculates $\boldsymbol{K}^e$ for each element. It then transforms the matrix from the local coordinate system into the global coordinate system and positions this matrix within the global stiffness matrix.

To transform from global coordinates to local coordinates, a rotation matrix ($\boldsymbol{R}$) is used, as shown in Equation 6.8.

$$\boldsymbol{u}^e = \boldsymbol{R}\boldsymbol{u} \tag{6.8}$$

The rotation matrix requires the angle between the global axes to the local axis, i.e. $\theta_{N,n}$. These angles are substituted into matrix $\boldsymbol{r}$, as seen in Equation 6.9. The $\boldsymbol{r}$ matrix is then substituted along the main diagonal in the $\boldsymbol{R}$ matrix, as seen in Equation 6.10.

$$\boldsymbol{r} = \begin{bmatrix} \cos\theta_{X,x} & \cos\theta_{Y,x} & \cos\theta_{Z,x} \\ \cos\theta_{X,y} & \cos\theta_{Y,y} & \cos\theta_{Z,y} \\ \cos\theta_{X,z} & \cos\theta_{Y,z} & \cos\theta_{Z,z} \end{bmatrix} \tag{6.9}$$

$$\boldsymbol{R} = \begin{bmatrix} r & 0 & 0 & 0 \\ 0 & r & 0 & 0 \\ 0 & 0 & r & 0 \\ 0 & 0 & 0 & r \end{bmatrix} \tag{6.10}$$

Equation 6.8 is then substituted into Equation 6.5, which results in Equation 6.11 and 6.12 after some matrix algebra has been preformed. The element's stiffness matrix can be calculated using the material and spoke properties. The rotation matrix can be calculated using the node's coordinates and the relationship between the local and global coordinate system. With $\boldsymbol{K}^e$ and $\boldsymbol{R}$ known, the global stiffness matrix can be calculated.

$$\begin{aligned} U_e &= \tfrac{1}{2}\boldsymbol{u}^{e,T}\boldsymbol{K}^e\boldsymbol{u}^e \\ &= \tfrac{1}{2}\boldsymbol{u}^T\boldsymbol{R}^T\boldsymbol{K}^e\boldsymbol{R}\boldsymbol{u} \\ &= \boldsymbol{u}^T\boldsymbol{K}\boldsymbol{u} \end{aligned} \tag{6.11}$$

$$\boldsymbol{K} = \boldsymbol{R}^T\boldsymbol{K}^e\boldsymbol{R} \tag{6.12}$$

6.4 Force Vector and Finite Element Solution

Three forces and three moments can be applied to each node. A vector named *Force* lists the forces applied at each node in numbered order. The forces in the wheel are applied at the node in the centre. The forces on the remaining nodes are set to zero.

With the force vector complete and the stiffness matrix calculated, the displacement vector can be calculated. The code passes the wheel structure as an argument and returns the values of the displacements and forces of the active degrees of freedom. The displacement's units are metres, while the rotation's units are radians.

6.5 Strain Calculation

The strain is calculated by simplifying the Green-Lagrange strain tensor using the assumptions made when using the Euler-Bernoulli beam formulation. The strain tensor for a 3-dimensional element is given in Equation 6.13 [25]. Since the beam is in equilibrium $\epsilon_{xy} = \epsilon_{yx}$, $\epsilon_{xz} = \epsilon_{zx}$ and $\epsilon_{yz} = \epsilon_{zy}$

The assumption that the cross-section remains orthogonal to the local x-axis and does not deform means that the Poisson contractions can be neglected, i.e. the Poisson's ratio is set to zero. This sets the normal strain in the local y- and z-directions, such that $\epsilon_{yy} = \epsilon_{zz} = 0$.

$$\boldsymbol{\epsilon} = \begin{bmatrix} \epsilon_{xx} & \epsilon_{xy} & \epsilon_{xz} \\ \epsilon_{yx} & \epsilon_{yy} & \epsilon_{yz} \\ \epsilon_{zx} & \epsilon_{zy} & \epsilon_{zz} \end{bmatrix} = \begin{bmatrix} \frac{\partial u_x}{\partial x} & \frac{1}{2}(\frac{\partial u_x}{\partial y} + \frac{\partial u_y}{\partial x}) & \frac{1}{2}(\frac{\partial u_x}{\partial z} + \frac{\partial u_z}{\partial x}) \\ \frac{1}{2}(\frac{\partial u_x}{\partial y} + \frac{\partial u_y}{\partial x}) & \frac{\partial u_y}{\partial y} & \frac{1}{2}(\frac{\partial u_y}{\partial z} + \frac{\partial u_z}{\partial y}) \\ \frac{1}{2}(\frac{\partial u_x}{\partial z} + \frac{\partial u_z}{\partial x}) & \frac{1}{2}(\frac{\partial u_y}{\partial z} + \frac{\partial u_z}{\partial y}) & \frac{\partial u_z}{\partial z} \end{bmatrix} \tag{6.13}$$

The displacement field at an arbitrary position x along the beam is given by Equation 6.14. This is derived from kinematic constraints as shown in Figure 6.4. The non-planar displacement caused by the torsional moment is accounted for by the *warping function* ($\omega(y, z)$). This warping function depends on the boundary (the y- and z-coordinates) of the cross-section.

$$\begin{aligned} u_x(x, y, z) &= u(x) + z\theta_y(x) - y\theta_z(x) + \omega(y, z)\tfrac{d\theta_x}{dx} \\ u_y(x, y, z) &= w(x) - z\theta_x(x) \\ u_z(x, y, z) &= v(x) + y\theta_x(x) \end{aligned} \tag{6.14}$$

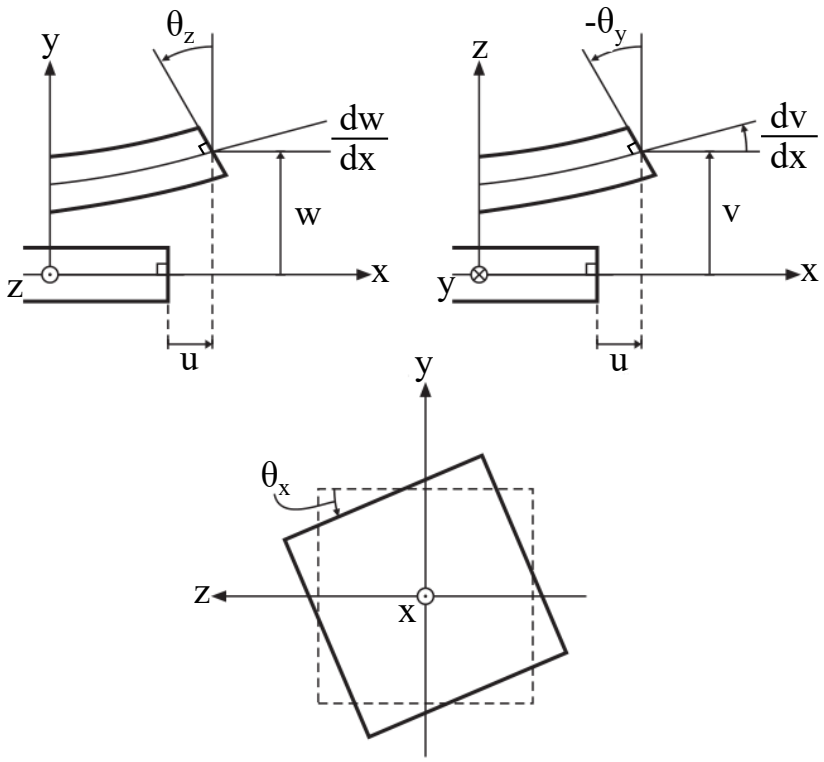


Figure 6.4: Kinematic constraints for a Euler-Bernoulli beam

The displacement field (Equation 6.14) is substituted into the strain tensor and then differentiated. This results in four unique components, as listed in Equations 6.15, 6.16, 6.17 and 6.18.

$$\epsilon_{xx} = \frac{du}{dx} + z\frac{d\theta_y}{dx} - y\frac{d\theta_z}{dx} + \omega\frac{d^2\theta_x}{dx^2} \tag{6.15}$$

$$\epsilon_{xy} = \epsilon_{yx} = \frac{1}{2}\left(\frac{dw}{dx} - \theta_z(x) + \frac{d\theta_x}{dx}\left(\frac{\partial\omega}{dy} - z\right)\right) \tag{6.16}$$

$$\epsilon_{xz} = \epsilon_{zx} = \frac{1}{2}\left(\frac{dw}{dx} + \theta_y(x) + \frac{d\theta_x}{dx}\left(\frac{\partial\omega}{dz} + y\right)\right) \tag{6.17}$$

$$\epsilon_{yz} = \epsilon_{zy} = \frac{1}{2}\left(\frac{dv}{dz} + \frac{dw}{dy}\right) \tag{6.18}$$

These equations can be further simplified by applying the assumption that the cross-sections remain plane and perpendicular to the local x-axis. This produces an additional kinematic constraint, where $\theta_y = -dv/dx$ and $\theta_z = dw/dx$. Substituting this into Equations 6.16 and 6.17, produces Equations 6.19 and 6.20. This assumption also leads to $dw/dz = dz/dy = 0$, and applying this to Equation 6.18 leads to $\epsilon_{yz} = 0$.

$$\epsilon_{xy} = \frac{1}{2}\frac{d\theta_x}{dx}\left(\frac{\partial\omega}{dy} - z\right) \tag{6.19}$$

$$\epsilon_{xz} = \frac{1}{2}\frac{d\theta_x}{dx}\left(\frac{\partial \omega}{dz} + y\right) \tag{6.20}$$

The torsional moment (M_x) that causes the beam to twist may be assumed to be *homogeneous*. This means that M_x, hence $d\theta_x/dx$, is constant throughout the element. This assumption relies on the fact that the torsional moment is not reacted at any point along the beam, and the only point that reacts to the torsional moment is at the opposite node. This assumption leads to $d^2\theta_x/dx^2 = 0$, which, after substituting into Equation 6.15, leads to Equation 6.21.

$$\epsilon_{xx} = \frac{du}{dx} + z\frac{d\theta_y}{dx} - y\frac{d\theta_z}{dx} \tag{6.21}$$

Equation 6.21 may written in matrix form where $\epsilon_{xx} = \boldsymbol{F}\boldsymbol{u}(x)$. $\boldsymbol{F}$ is known as the *deformation gradient matrix* and shown in Equation 6.22, and $\boldsymbol{u}(x)$ is the displacement vector at point x along the beam. Substituting Equation 6.3 into this leads to Equation 6.23. Let $\boldsymbol{B} = \boldsymbol{F}\boldsymbol{N}$, which is known as the *strain-displacement* matrix, as shown in Equation 6.24.

$$\boldsymbol{F} = \begin{bmatrix} \frac{d}{dx} & -y\frac{d^2}{dx^2} & z\frac{d^2}{dx^2} \end{bmatrix} \tag{6.22}$$

$$\epsilon_{xx} = \boldsymbol{F}\boldsymbol{N}\boldsymbol{u}^e \tag{6.23}$$

$$\boldsymbol{B} = \boldsymbol{F}\boldsymbol{N} \tag{6.24}$$

The axial strain at any point x can now be calculated by multiplying the *strain-displacement* matrix with the element displacement matrix. With the nodal displacements it is possible to return the axial displacement at any point along the beam.

The code calculates the global displacements of the beam in question. The global displacements are then rotated back to the local spoke coordinate system. These displacements are multiplied with the *strain-displacement* matrix, returning a scalar value which is the axial strain.

6.6 Stress Calculation

The axial strain can be used to calculate the stress and when compared to the endurance strength of the material can be used to compute the factor of safety.

The axial strain calculated in the previous section does not account for the shear strain. However, the angle of twist is known along the spoke's local X axis. Thus, the shear strain

may be calculated using $\tau_{xy} = G\theta_x$. The shear strain in the other planes are assumed to be zero, $\tau_{yz} = \tau_{zx} = 0$

The axial strain (ϵ_{xx}) causes strain in the x- and z-directions through the Poison's ratio. This is calculated as follows $\epsilon_{yy} = \epsilon_{zz} = -\nu\epsilon_{xx}$.

The stress in each direction is calculated by multiplying the strain with the material's Young's modulus. This stress is substituted in Equations 6.25 and 6.26 to calculate the equivalent von Mises (σ') and principal stress (σ_P), respectively [14]. The three principal stresses are the three roots to Equation 6.26.

$$\sigma' = \frac{1}{\sqrt{2}}\Big[(\sigma_x - \sigma_y)^2 + (\sigma_y - \sigma_z)^2 + (\sigma_z - \sigma_x)^2 + 6(\tau_{xy}^2 + \tau_{yz}^2 + \tau_{zx}^2)\Big]^{1/2} \tag{6.25}$$

$$\begin{aligned}\sigma^3 - (\sigma_x + \sigma_y + \sigma_z)\sigma^2 + (\sigma_x\sigma_y + \sigma_x\sigma_z + \sigma_y\sigma_z - \tau_{xy}^2 - \tau_{yz}^2 - \tau_{zx}^2)\sigma - \\ (\sigma_x\sigma_y\sigma_z + 2\tau_{xy}^2\tau_{yz}^2\tau_{zx}^2 - \sigma_x\tau_{yz}^2 - \sigma_y\tau_{zx}^2 - \sigma_x\tau_{xy}^2) = 0\end{aligned} \tag{6.26}$$

The alternating and midrange stresses are needed to determine the fatigue strength of the wheel. This is computed by repeating the von Mises and principal stress calculations to determine the maximum and minimum stress experienced by the wheel during a full revolution.

Lastly, the ASME factor of safety can be calculated using the alternating and midrange stress and the material's strength properties in Equation 6.27 [14]. The ASME factor of safety was used as it is less conservative and more accurate than the Modified Goodman, Smith, Watson and Topper (SWT) and Soderberg approaches.

$$n_{ASME} = \left[\left(\frac{\sigma_a}{S_e}\right)^2 + \left(\frac{\sigma_m}{S_y}\right)^2\right]^{-1/2} \tag{6.27}$$

The safety factor provides a single number to use in comparisons between different load cases and wheel types with respect to the material's endurance limit. If the safety factor is below 1, then it is likely that the part will fail within the number of cycles that the endurance strength was tested for.

7 Insights from the Simplified Model

7.1 Comparison with Experimental Results

In this section, each of the wheels tested experimentally was analysed using the simplified model. The orientation (θ) of the primary spoke was varied from $\theta = 0°$ to $\theta = 360°$ as in the experiment. The strain calculated by the simplified model was then compared to the experimental results.

Each wheel was simplified using four geometric properties; the inner hub diameter, outer rim diameter, spoke angle (β), and the number of spokes. The inner hub diameter is the diameter that the spokes connect onto the central portion of the wheel. The outer rim diameter is the diameter that the spokes connect to the outer rim. The spoke angle (β) is the angle between a line through the inner node and a radial line passing through the outer node. These parameters are listed in Table 7.1. The relationship between the nodes and elements, when the primary spoke is at $\theta = 0°$, may be seen in Figure 7.1 for each wheel.

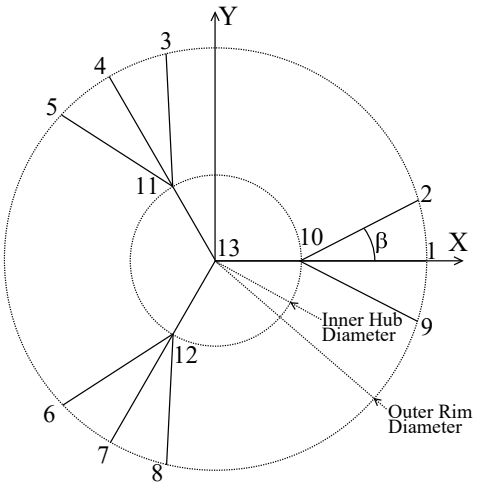
Table 7.1: Critical wheel geometry

Parameter	9 Spoke ORW	5 Spoke CRW	7 Spoke FW
β	45°	27°	44°
Inner hub diameter	117 mm	123 mm	140 mm
Outer rim diameter	400 mm	390 mm	382 mm
Number of spokes	9	5	7

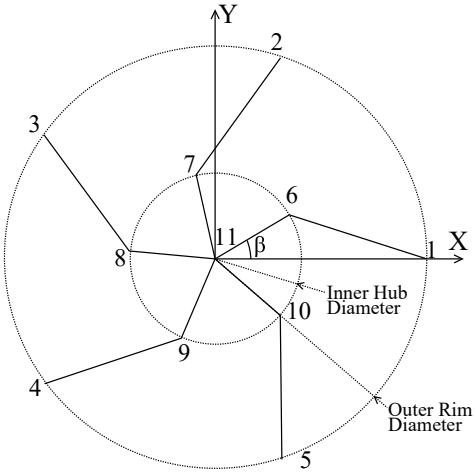
Each load case was decomposed into the force and moment components at the centre of the wheel. These components were applied at the centre node of each simplified model.

An element set was created with *hub elements* that connected the spokes to the centre. These "inner spokes" were made an order of magnitude stiffer than the spokes to model the high stiffness of the inner hub of the wheel that holds the brake discs and bearings.

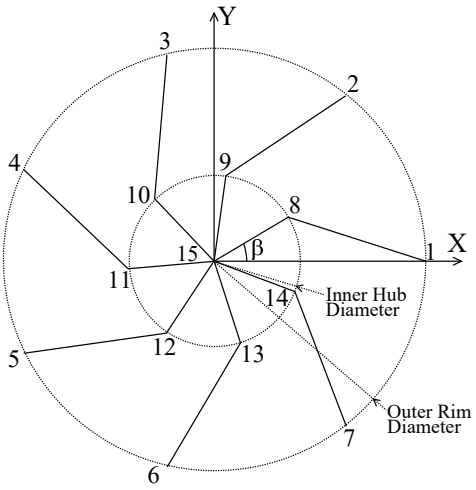
The outer spoke nodes were fixed (both translational and rotational DOFs were constrained) which most accurately modelled the attachment to the rim which is rigidly constrained in the experimental set-up.



(a) 9 Spoke ORW



(b) 5 Spoke CRW



(c) 7 Spoke FW

Figure 7.1: Diagram of elements and nodes of simplified model with $\theta = 0°$
(a) 9 Spoke ORW with nodes 1 to 9 fixed in all degrees of freedom
(b) 5 Spoke CRW with nodes 1 to 5 fixed in all degrees of freedom
(c) 7 Spoke FW with nodes 1 to 7 fixed in all degrees of freedom

The spoke strains calculated using the simplified model are compared to the FEA and experimental results in Figure 7.2 and Figure 7.3 for the bending and torsional load case respectively.

In the bending load case, the strain from the simplified model follows the same sinusoidal trend as seen in the FEA and experimental results. The difference between the simplified model and the FEA simulation was largest for the 9 spoke ORW. The 5 spoke CRW and the 7 spoke FW had differences of 21 % between the simplified model and the FEA simulation.

In the torsional load case, the 7 spoke FW and the 9 spoke ORW had the smallest error, while the 5 spoke CRW had the largest error. These errors were larger than the bending load case.

The strain was under estimated by the simplified model when compared to other the other results.

The difference between the simplified model and FEA and experimental results is partially due to the constant spoke cross-section assumption made with the simplified model. This is supported by the fact that the largest difference occurred in the wheel with the most complex spoke geometry, and the smallest error occurred in the wheel with the simplest spoke geometry. This will be further examined in Section 7.2.

Another reason for the difference is due to the Euler-Bernoulli beam formulation. This formulation is not shear-deformable, leading to a more rigid wheel. This leads to a lower strain value. A more accurate beam formulation was developed by Timoshenko. This formulation incorporates an additional differential equation that does not constrain the cross-section to be orthogonal to the neutral axis. If a Timoshenko beam formulation was used, the strain may have been closer to that of the FEA and experimental results.

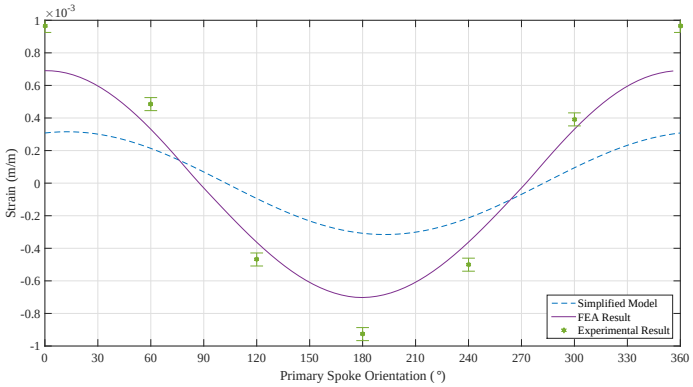
Goerguelue studied the difference between the Euler-Bernoulli and Timoshenko formulation [26]. He found that the difference between the two formulations is more pronounced for beams with a low aspect ratio. He defined the slenderness ratio of the beam to characterise the difference between the Euler-Bernoulli and Timoshenko formulation. The slenderness ratio is calculated using Equation 7.1. As an example, the spoke of the 5 spoke CRW has a slenderness ratio of 34, which translates into an difference of 8.6%.

$$Slenderness\ Ratio = \frac{GAL^2}{EI} \tag{7.1}$$

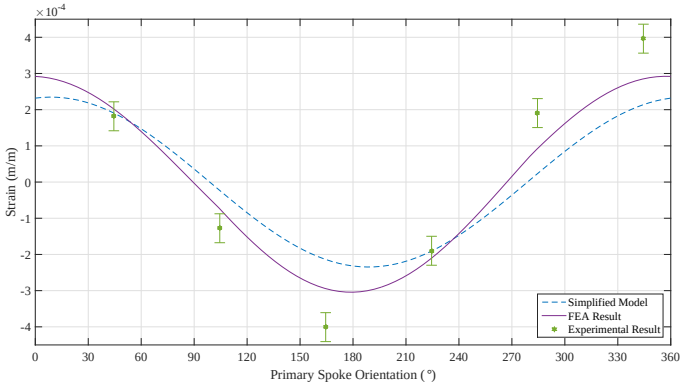
The simplified model correctly represents the trend and order of magnitude of the strain experienced by the wheel. The simplified model estimates the mechanics and overall behaviour of the wheel closely and can be used to provide valuable insight into improving the design of wheels.

The accuracy of the simplified model could be increased by using the Timoshenko formulation. The Timoshenko formulation introduces a differential equation that is an order higher than the Euler-Bernoulli formulation [27] [28]. The accuracy of the simplified model may be further increased by using multiple elements along each spoke that would capture the changing spoke cross-section.

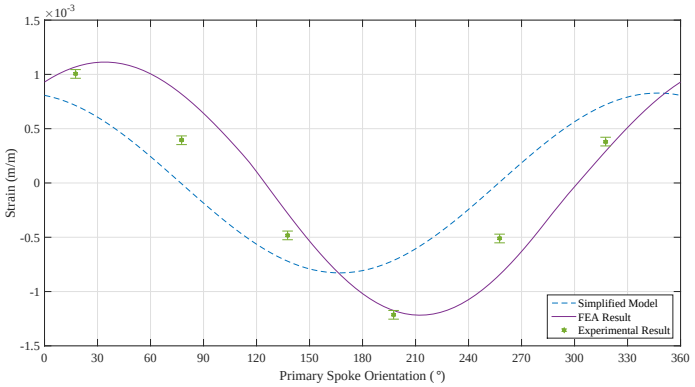
This added complexity was considered unnecessary as the simplified model captured the wheel behaviour allowing insights to the design of wheels to be developed.



(a) 9 Spoke ORW under bending load of 1 195 $N \cdot m$ at $x = 117\ mm$

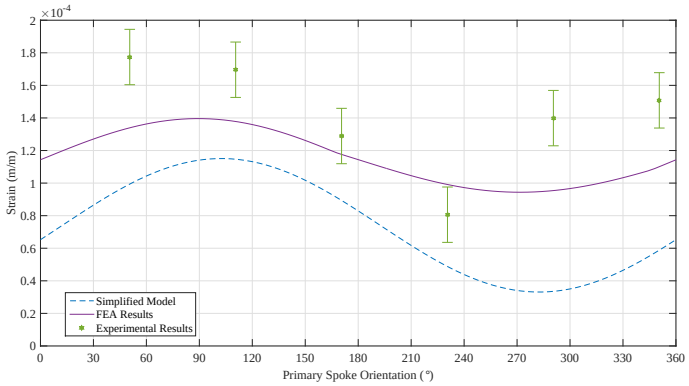


(b) 5 Spoke CRW under bending load of 1 340 $N \cdot m$ at $x = 125\ mm$

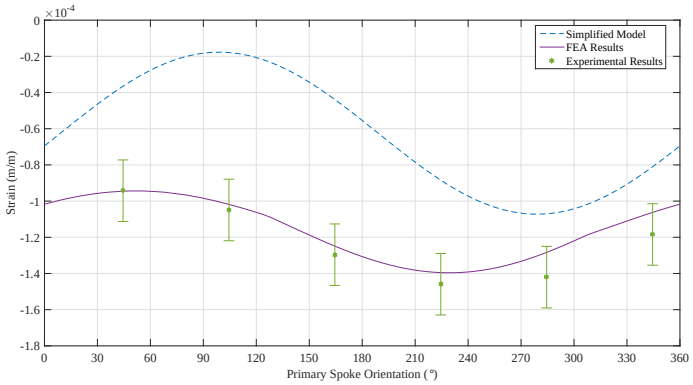


(c) 7 Spoke FW under bending load of 1 402 $N \cdot m$ at $x = 102\ mm$

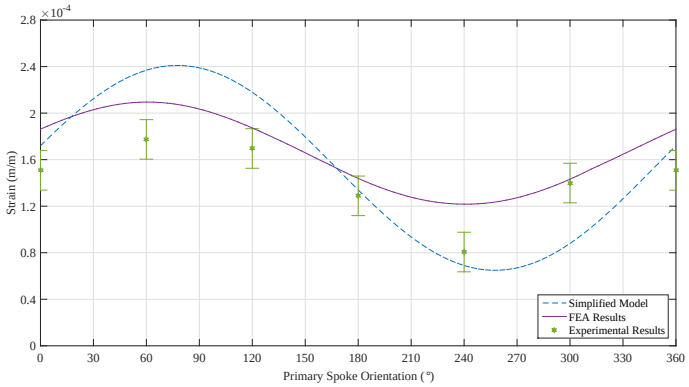
Figure 7.2: Strain versus spoke orientation (θ) for
(a) 9 Spoke ORW under bending load of 1 195 $N \cdot m$ at $x = 117\ mm$
(b) 5 Spoke CRW under bending load of 1 340 $N \cdot m$ at $x = 125\ mm$
(c) 7 Spoke FW under bending load of 1 402 $N \cdot m$ at $x = 102\ mm$



(a) 9 Spoke ORW under torsional load of 736 $N \cdot m$ at $x = 80\ mm$



(b) 5 Spoke CRW under torsional load of 736 $N \cdot m$ at $x = 123\ mm$



(c) 7 Spoke FW under torsional load of 736 $N \cdot m$ at $x = 100\ mm$

Figure 7.3: Strain versus spoke orientation (θ) for
(a) 9 Spoke ORW under torsional load of 736 $N \cdot m$ at $x = 80\ mm$
(b) 5 Spoke CRW under torsional load of 736 $N \cdot m$ at $x = 123\ mm$
(c) 7 Spoke FW under torsional load of 736 $N \cdot m$ at $x = 100\ mm$

7.2 Comparison with an Idealised Wheel

The simplified model approximates each spoke of a wheel into a beam with a constant cross-section. The following section studies the effect of assuming the spoke has a constant cross-section. This assumption was tested by comparing the FEA results of an idealised hollow cylindrical spoke wheel with the simplified model of the same wheel. The idealised 5 spoke CRW may be seen in Figure 7.4.

Firstly, an idealised 5 spoke conventional rear wheel was modelled using the same FEA simulation method as the previous wheels. This wheel had no additional features, such as fillets, chamfers or draft angles as seen in the previous wheels. The spoke of the idealised wheel had the average spoke cross-sectional area of the previous three wheels that were studied. The results of the idealised spoke FEA and the simplified model results are compared in Figure 7.5 for the bending and torsional load cases.

In additional to the straight spoke wheel, a wheel with tapered spokes was simulated. The tapered spokes had the identical midpoint cross-section as the straight spoke. This meant that both the tapered and straight spoke wheels had the same mass. The spokes had the same change in area moment of inertia as the tested wheels. This was found to be 0.0315 mm^4 per millimetre of spoke length. This is equivalent to a 6° taper for a hollow cylinder.

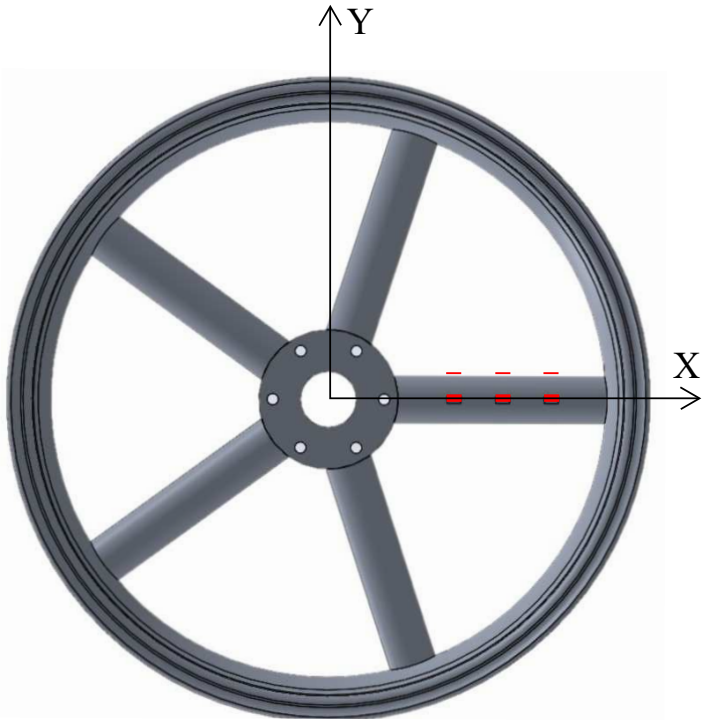


Figure 7.4: Idealised straight spoke wheel

For the bending load case, the average difference between the strains calculated using the idealised straight spoke FEA model and the simplified model is 0.5%, while the average difference for the idealised tapered spoke is 13.4%. This is shows that the constant cross-section assumption increases the error.

For the torsional load case, the average difference between the strains calculated using the the idealised straight spoke FEA model and the simplified model is 5.6%, while the average difference for the idealised tapered spoke is 57.4%. For the torsional load case the constant cross-section assumption causes much larger error than the bending load case.

The strain in the idealised tapered spoke wheel is lower than the idealised straight spoke wheel by 15% and 60% for the bending and torsional load case, respectively. While the tapered spoke has the same mass as the straight spoke, it will have a higher factor of safety than the straight spoke wheel thus being a safer design. Furthermore analysing the tapered spoke wheel assuming the spoke to be straight will be conservative.

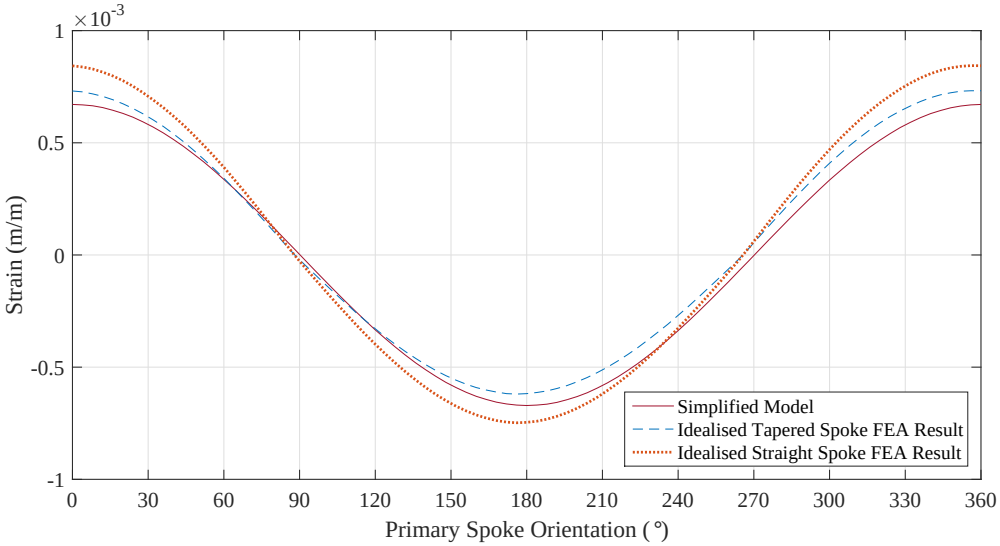
7.3 Using the Simplified Model to Develop Insight into Wheel Design

The simplified model of a wheel allows for the quick prediction of the strain for many spoke configurations and sizes. This strain can be used to calculate the stress and the factor of safety of the wheel, as described in Section 6.6. The factor of safety is a single number that allows the fatigue life of different wheel types to be compared.

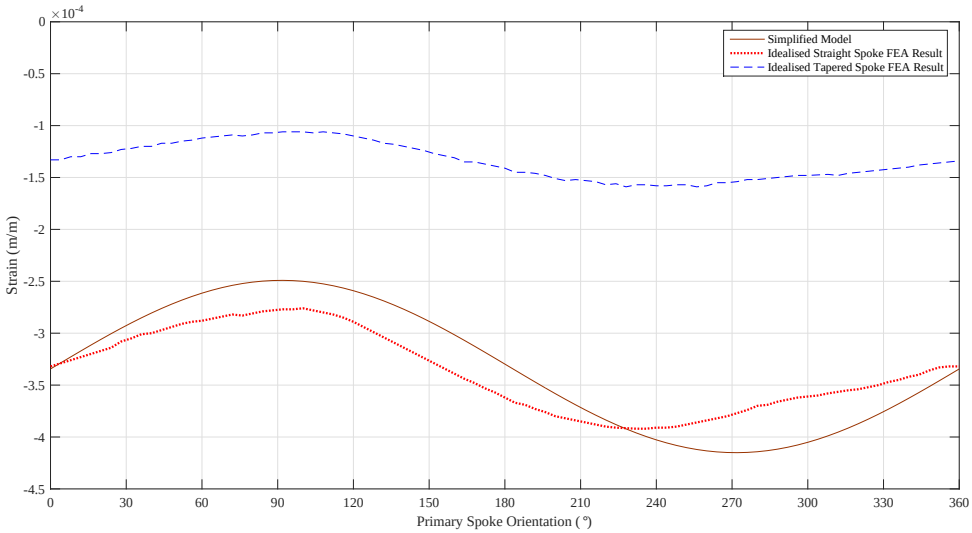
A simplified wheel based on the 5 spoke CRW was used to determine the effect of various design decisions. The simplified wheel remained a 17 inch aluminium wheel, with the material properties discussed in earlier sections. The spoke angle (β) was set to $\beta = 0°$ such that the spokes follow a radial line.

The factor of safety versus the number of spokes is plotted in Figure 7.6(a). Each run added an identical spoke to the wheel and then recalculated the factor of safety. The factor of safety was calculated using the maximum and minimum von Mises stress experienced during one full rotation of the wheel, and determined the alternating and midrange stress.

There is a linear relationship between the factor of safety and number of spokes for both load cases. The torsional load case has a notably higher safety factor than the bending load case. This was expected when the experimental results were evaluated.



(a) Bending load case

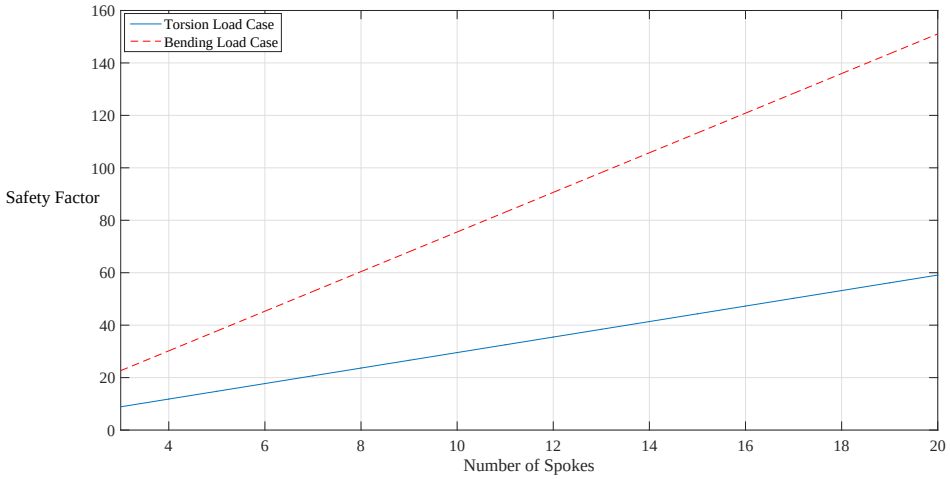


(b) Torsional load case

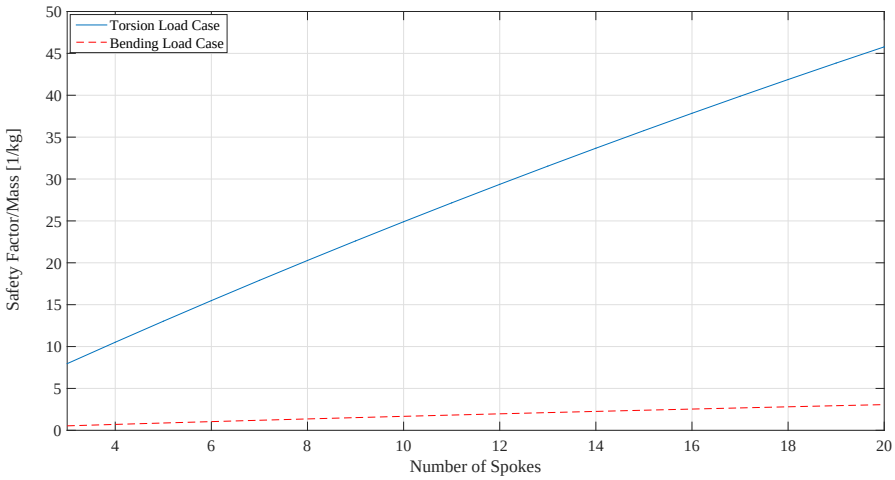
Figure 7.5: Comparison of simplified model to idealised spoke FEA results under:
(a) Bending load case
(b) Torsional load case

Increasing the number of spokes, increases the factor of safety of the wheel. However, the additional spokes increase the mass of the wheel. The mass of the wheel is critical to the performance of the vehicle as a whole. To quantify the effect of the additional mass, the factor of safety was normalised with the wheel's mass, and plotted in Figure 7.6(b).

The normalised factor of safety still increases with increasing number of spokes but the increase with number of spokes becomes marginal with the bending load case seeing the smallest increase. The results show that the addition of spokes while keeping the wheel's mass constant has a small effect on the fatigue strength of the wheel design.



(a) Number of spokes versus ASME factor of safety



(b) Number of spokes versus ASME factor of safety normalised with the mass of the wheel

Figure 7.6: Comparison of the number of spokes with:
(a) ASME factor of safety
(b) ASME factor of safety normalised with the mass of the wheel

The outer wheel diameter would be typically determined by the dynamic handling requirements of the vehicle. Hence, only the inner hub diameter of the two diameters may realistically be varied. The spoke length is inversely related to the inner hub diameter; i.e. a larger inner hub diameter results in a shorter spoke. Thus, a change in the inner hub diameter is representative of a change in the spoke length.

Figure 7.7(a) and (b) plots the normalised factor of safety with respect to the effect of the inner hub diameter for different numbers of spokes for the bending and torsional load case respectively. The inner hub diameter varied from 1 mm to 300 mm, while the outer diameter was fixed at 390 mm (typical of a 17 inch wheel diameter).

In the bending load case, shown in Figure 7.7(a), a smaller hub diameter (i.e. a longer spoke) results in a higher normalised factor of safety. The results show that reducing the hub diameter increases the fatigue strength of the wheel and uses material more effectively for the bending load case.

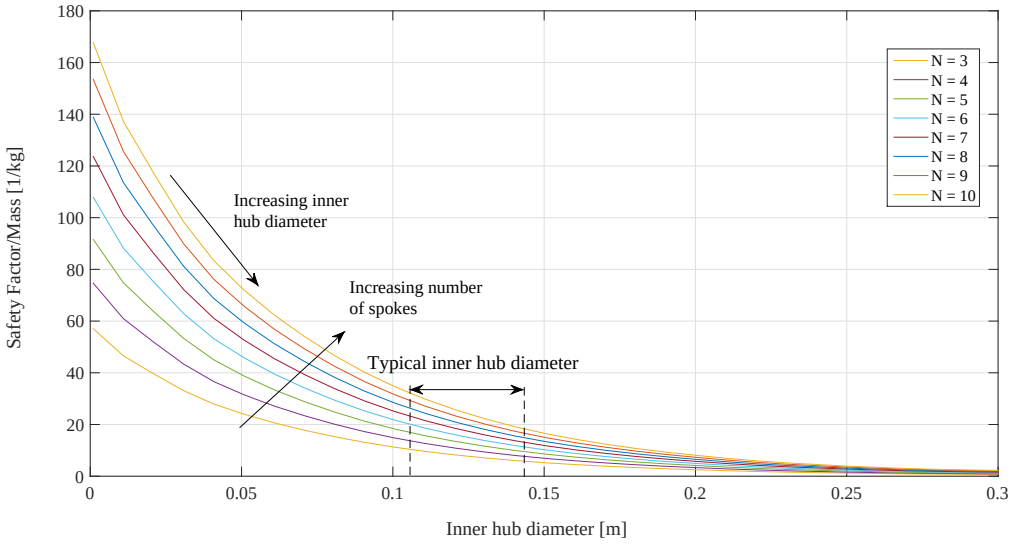
In the torsional load case, shown in Figure 7.7(b), there was an optimum inner hub diameter which maximizes the normalised factor of safety. The optimum inner hub diameter for a 10 spoke wheel was shown to be 50 mm (or a spoke length of 170 mm). This optimal value decreases slightly as the number of spokes decrease. For a wheel with 3 spokes, the optimum inner hub diameter was shown to be 40 mm (or a spoke length of 175mm). Typical inner hub diameters are 110 mm to 140 mm as shown in the figure. Thus decreasing the inner hub diameter from a typical inner hub diameter will increase the wheel's fatigue strength and use material more effectively for the torsional load case.

In Figure 7.8(a) and (b) plots the normalised factor of safety with respect to the spoke angle (β) for different numbers of spokes for the bending and torsional load case respectively. The spoke angle was varied from $\beta = 0^\circ$ to $\beta = 110^\circ$.

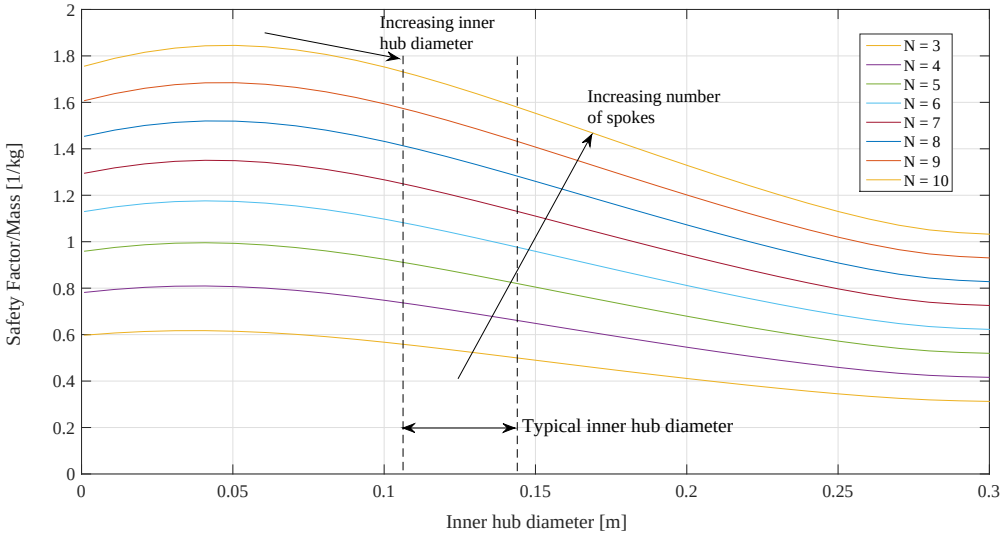
In the bending load case, there is a slight increase in the normalised factor of safety at small spoke angles and the factor of safety increase gradient gets larger as β increases. There exists a maximum at $\beta = 102^\circ$ and a decrease thereafter.

In the torsional load case, there is also an increase in normalised factor of safety with respect to the spoke angle. A maximum occurs at $\beta = 90^\circ$, at $\beta = 90^\circ$ the spokes would all be loaded in axial tension which is the most effective use of material as the strain is constant through the cross-section.

The results show that adding spoke angle increases the strength of the wheel or stated differently uses the spoke material more effectively.



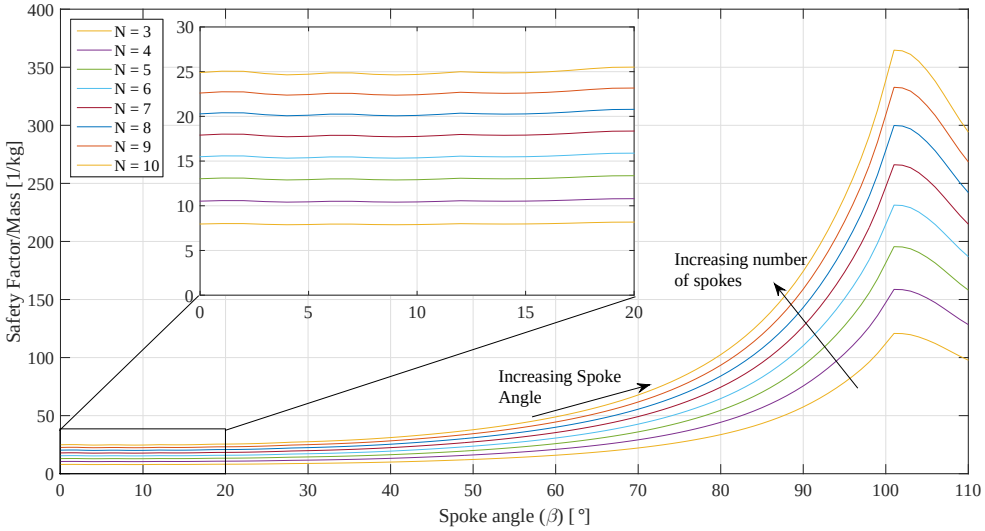
(a) Bending load case



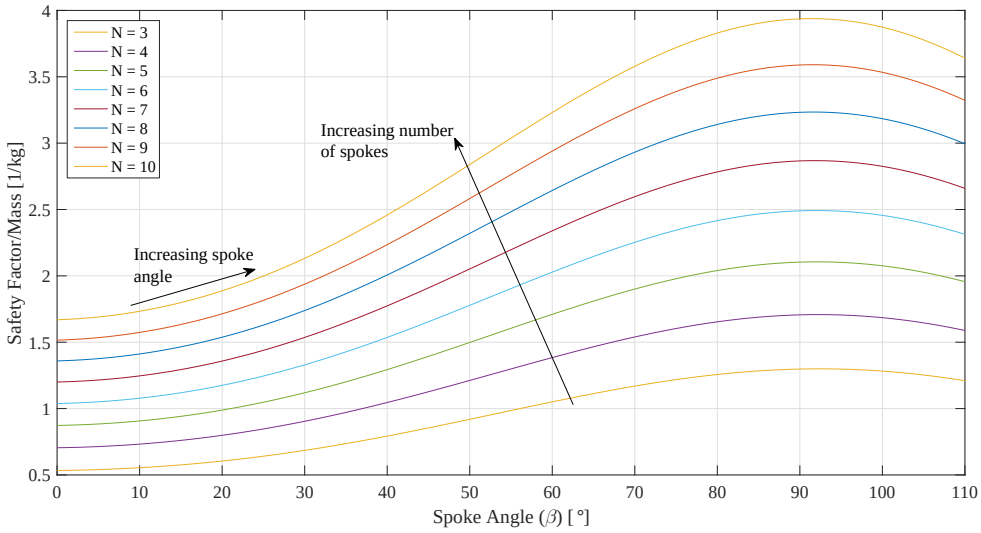
(b) Torsional load case

Figure 7.7: The effect of the inner hub diameter with the safety factor normalised with wheel mass with $\beta = 0°$ for the:
(a) Bending load case
(b) Torsional load case

The node positions for a 5 spoke wheel with different spoke angles is shown in Figure 7.9. Figure 7.9(a) shows the layout that produced the maximum normalised factor of safety in the torsional load case. Figure 7.9(b) shows the layout that produced the maximum normalised factor of safety in the bending load case. When $\beta \geq 110°$, the spokes cross one another as seen in Figure 7.9(c). This would not be physically feasible.

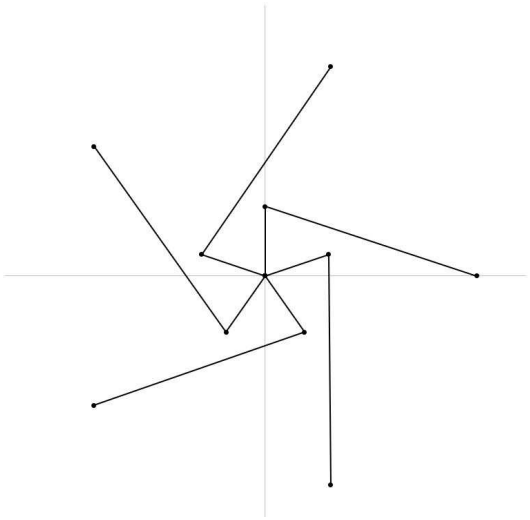


(a) Bending load case

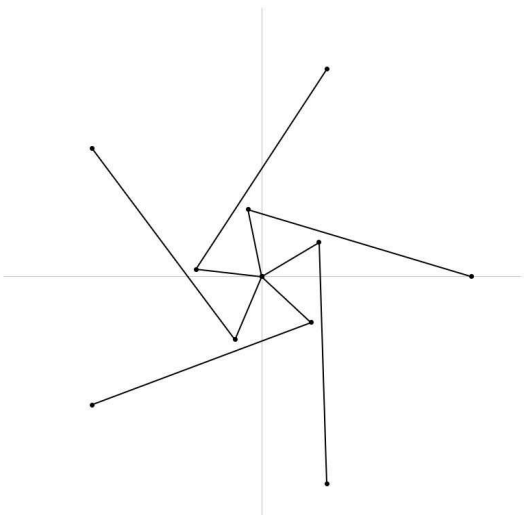


(b) torsional load case

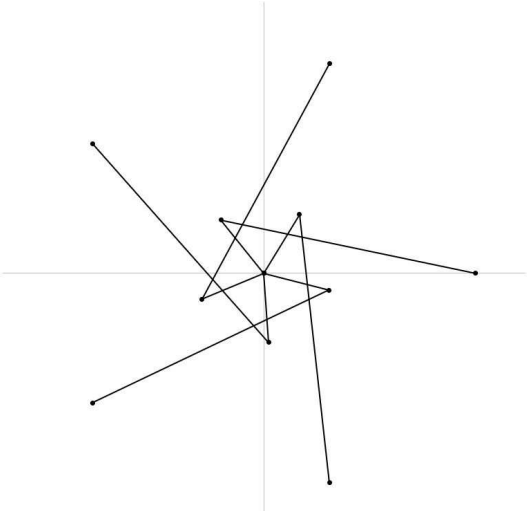
Figure 7.8: The effect of the spoke angle (β) with the safety factor normalised with wheel mass for the:
(a) Bending load case
(b) Torsional load case



(a) $\beta = 90°$



(b) $\beta = 102°$



(c) $\beta = 130°$

Figure 7.9: Diagram of elements and nodes of simplified model with:
(a) $\beta = 90°$
(b) $\beta = 102°$
(c) $\beta = 130°$

7.4 Comparison of the Alternating Torsion, Bending Moment and Radial Fatigue Tests

In this section the three fatigue tests typically included in a wheel strength standard are examined using the simplified model of the three experimental wheels. The maximum static load rating was used to calculate the required load for each wheel as described in Section 3.5. These loads are shown in Table 7.2.

The radial load case simulates the radial fatigue test. This laboratory test acts as a proxy for straight-ahead driving of the vehicle. The maximum static load rating was multiplied by a factor of 2.25, as per the ISO 8644:2006 standard. This load was applied in the global Y axis and the primary spoke's orientation increased, so as to simulate a rotating wheel.

The bending and torsional load cases were applied using a pure couple. This is different to how test rigs apply the load; test rigs apply a known load using a moment or load arm.

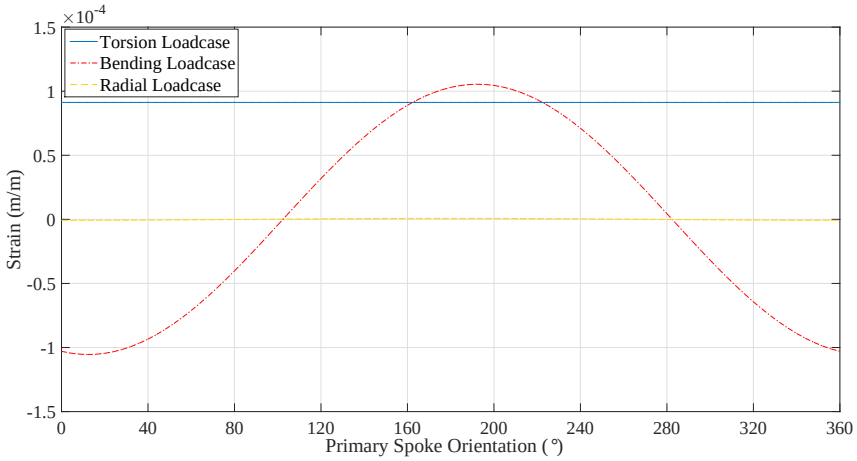
Table 7.2: Required fatigue wheel loads

Wheel	Load Rating	Bending Load	Torsional Load	Radial Load
9 Spoke ORW	250 kg	418 $N \cdot m$	853 $N \cdot m$	5518 N
5 Spoke CRW	250 kg	418 $N \cdot m$	853 $N \cdot m$	5518 N
7 Spoke FW	150 kg	222 $N \cdot m$	453 $N \cdot m$	3311 N

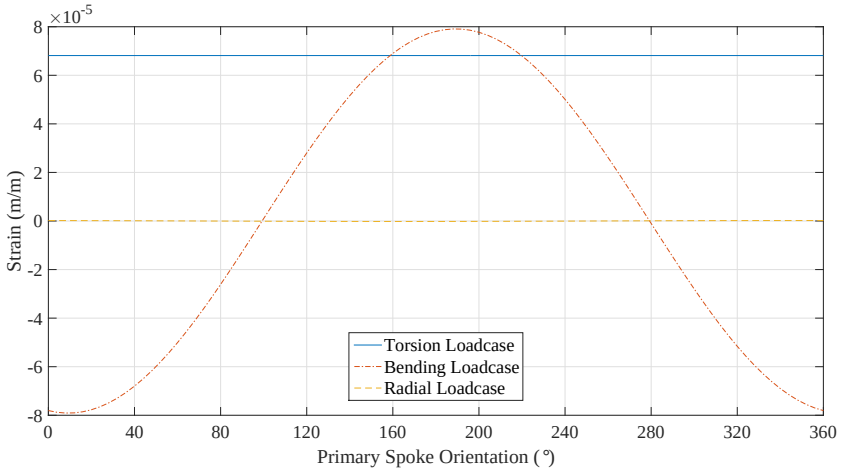
Figure 7.10 plots the strain versus spoke orientation for each load case for the three wheels. For each wheel the bending load case produced the highest strain, which was on average 21 % higher than the torsional load case. The strain produced by the radial load case was three orders of magnitude smaller than the other load cases, thus the strain produced was insignificant in the three wheels.

The strain in the torsional load case was constant with the spoke's orientation. This was in contrast to what was seen in the experiment. This change was brought about because a pure couple was applied instead of a moment and force, as seen in the load generated by the test rig. A pure couple was more inline with the intentions of the wheel test standard.

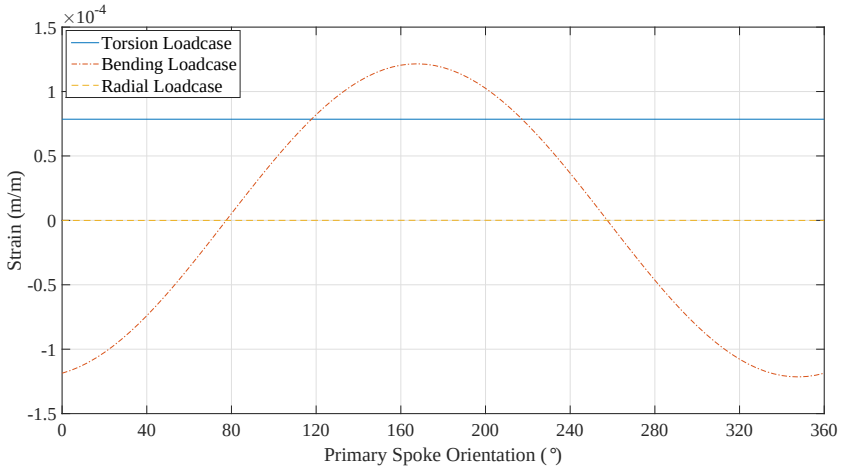
The results in Figure 7.10 confirm that dynamic cornering or bending moment fatigue test is of primary concern as stated by Wang [5] and Riesner [12]. The simpified model has quantified this by showing that the bending moment test generates a strain 21 % higher than the torsional test.



(a) 9 Spoke ORW



(b) 5 Spoke CRW



(c) 7 Spoke FW

Figure 7.10: Strain versus spoke orientation (θ) for
(a) 9 Spoke ORW, bending = 418 $N \cdot m$, torsion = 853 $N \cdot m$ and radial = 5518 N
(b) 5 Spoke CRW, bending = 418 $N \cdot m$, torsion = 853 $N \cdot m$ and radial = 5518 N
(c) 7 Spoke FW, bending = 222 $N \cdot m$, torsion = 453 $N \cdot m$ and radial = 3311 N

8 Conclusions

The following may be concluded from the experimental results:

- The strain in a wheel can be accurately measured for bending moment and torsional loads. The strain varies sinusoidally with wheel orientation.
- For the wheels tested, the bending load case produced a strain that was 65 % higher than the torsional load case, for a given maximum static load rating.
- For the wheels tested, when the strain was normalised with respect to the moment applied to the wheel in each load case, the bending load case was 32% higher than the torsional load case.
- The bending load case is more critical to the fatigue strength than the torsional load case. This is not only because the stresses are higher in the case of bending but because the bending load case produces a fully reversed stress on the wheel during a revolution whereas the torsional load case does not.

The following may be concluded from the finite element analysis results:

- This finite element analysis can calculate the strain to within 20 % of the experimental results. The greatest difference occurs at the maximum and minimum values. The difference is within 10 % of the experimental results in orientations away from the sinusoidal peaks.
- The accuracy of the finite element analysis would be increased through more accurate CAD modelling and by using the experimentally measured properties of the material used in the wheel design.
- The finite element results closely follows the sinusoidal trend of the experimental results for all wheels in both load cases.

The experimental and finite element results were used to develop a simplified model to develop insight into the required wheel design to ensure wheels pass the bending moment and alternating torsion tests. The following insights can be concluded from the simplified model:

- The simplified model calculates the strain to within 30 % of the experimental results, with the biggest difference occurring at the maximum and minimum.
- The difference of the simplified model reduces to 11 % when the complexities in the spoke geometry (e.g. taper) are removed.
- The simplified model shows that there is an increase in the normalised factor of safety (or the strength of the wheel) for a given amount of material when (1) adding more spokes, (2) reducing the hub diameter and (3) increasing the spoke angle.
- The simplified model predicts that the strain is 21 % higher in the bending load case over the torsional load case, whereas the radial load case produce negligible load in the spokes.

9 Recommendations

The following recommendations are made for future work:

- Preform more than six increments in spoke orientation to better define the sinusoidal trend of experimental results.
- Obtain accurate CAD models and material properties from wheel manufacturers or through other methods, such as 3D scanning and material tests.
- Investigate the effect of the shear-undeformable assumption on the simplified model. The formulation is known as Timoshenko beam element and is particularly more accurate than Euler beam elements for short, stubby beams.

References

[1] TUV Rheinland, "TUV Guidelines For The Testing And Inspection of Custom Wheels For Motor Vehicles And Their Trailers," 1998.

[2] ISO, "ISO3006: Road Vehicles - Passenger Car Wheels for Road Use - Test Methods," 2005.

[3] ISO, "ISO7141: Road Vehicles - Light Alloy Wheels - Impact Test," 2005.

[4] ISO, "ISO8644: Motorcycles - Light Alloy Wheels - Test Method," 2006.

[5] X. Wang and X. Zhang, "Simulation of Dynamic Cornering Fatigue Test of a Steel Passenger Car Wheel," *International Journal of Fatigue*, vol. 32, pp. 434–442, 2010.

[6] J. Shear, "Personal Conversation - Head Engineer - BlackStone Tek," 2016.

[7] H. Karandikar and W. Fuchs, "Fatigue Life Prediction for Wheels by Simulation of the Rotating Bending Test," *SAE Technical Paper Series*, 1990.

[8] U. Kocabicak and M. Firat, "Numerical Analysis of Wheel Cornering Fatigue Test," *Engineering Failure Analysis*, vol. 8, pp. 339–354, 2001.

[9] P. R. Raju, B. Satyanarayana, K. Ramji, and K. S. Babu, "Evaluation of Fatigue Life of Aluminium Alloy Wheels Under Bending Loads," *Fatigue & Fracture of Engineering Materials & Structures*, vol. 32, pp. 119–126, 2009.

[10] R. Shang, W. Altenhof, H. Hu, and N. Li, "Rotary Fatigue Analysis of Forged Magnesium Road Wheels," *SAE International Journal of Material Manufacturing*, vol. 1, no. 1, 2008.

[11] Z.-G. Zheng, T. Sun, X.-Y. Xu, S.-Q. Pan, and S. Yuan, "Numerical Simulation of Steel Wheel Dynamic Cornering Fatigue Test," *Engineering Failure Analysis*, vol. 39, pp. 124–134, 2014.

[12] M. Riesner and R. DeVries, "Finite Element Analysis and Structural Optimization of Vehicle Wheels," *SAE Technical Paper Series*, no. 830133, 1983.

[13] Kyowa, "Kyowa Strain Gauge Catalog," *SAE Technical Paper Series*, vol. 101I-U1, no. 0129.

[14] R. G. Budynas and J. K. Nisbett, *Shigley's Mechanical Engineering Design*. MacGraw Hill, 9 ed., 2008.

[15] ETRTO, "ETRTO Standards Manual," tech. rep., Brussels, 2003.

[16] Ozgun, "Mechead - contact types and behaviours in ansys," 2018.

[17] A. J. M. Ferreira, *MatLab Codes for Finite Element Analysis*. Portugal: Springer, 2009.

[18] A. Khennane, *Finite Element Analysis using MatLab and Abaqus*. New Wales: Taylor and Francis Group, 2013.

[19] European Aluminium Association, "Applications - Chassis & Suspension - Wheels," *THE Aluminium Automotive MANUAL*, pp. 1–22, 2011.

[20] Z. Li, A. A. Luo, Q. Wang, H. Zou, J. Dai, and L. Peng, "Fatigue characteristics of sand-cast AZ91D magnesium alloy," *Journal of Magnesium and Alloys*, vol. 5, no. 1, pp. 1–12, 2017.

[21] A. Gryguc, S. K. Shaha, H. Jahed, M. Wells, B. Williams, and J. McKinley, "Tensile and fatigue behaviour of as-forged AZ31B extrusion," *Frattura ed Integrita Strutturale*, vol. 10, no. 38, pp. 251–258, 2016.

[22] L. Andersen and S. R. K. Nielsen, *Elastic Beams in Three Dimensions*. Denmark: Aalborg University, 2008.

[23] O. A. Bauchau and J. I. Craig, *Euler-Bernoulli beam theory*, pp. 173–221. Dordrecht: Springer Netherlands, 2009.

[24] C. Felippa, *The TL Plane Element: Formulation*, pp. 11.1–11.23. Boulder: University of Colorado, 2017.

[25] T. Wierzbicki, "The Concept of Strain," *Structural Mechanics*, no. 2.080J, 2013.

[26] U. Goerguelue, "The Difference between Euler-Bernoulli and Timoschenko," *Beam Theories*.

[27] B. Bettig, "Unit 2 - Timoshenko Beam Model," in *Rotordynamics*, Michigan: Michigan Technological University.

[28] Y. Luo, "An Efficient 3D Timoshenko Beam Element with Consistent Shape Functions," *Advanced Theory of Applied Mechanics*, vol. 1, no. 3, pp. 95–106, 2008.

Appendix A MatLab Code

Wheel Inputs

```
function p = WheelInputs( text, theta )
%WheelInputs Gives the required inputs for the specified wheel
%   text specifies the wheel.
%   theta specifies the angle in radians to the primary spoke along the
%   positive z direction.
%   if statement decides on the input .
%   return a structure file type, p.

% uses single node in center with 1000x stiffer hub elements connecting
% spokes to center at the inner hub diameter. All the outer nodes are fixed
% in all directions and rotations

p = struct; % creates array structure to store wheel data in

if strcmp(text,'5 spoke CRW') % 5 Spoke CRW Inputs
    OuterRimDiameter = 0.38962; % in m
    InnerHubDiameter = 0.12277; % in m
    beta = (360-20) * pi/180;
% angle of spoke from line between center node to outer rim node
    p.SpokesNo = 5;
    p.Connection = [1 6;2 7;3 8;4 9;5 10;6 11;7 11;8 11;9 11;10 11];
% shows which nodes are connected via elements
    p.ElementNo = size(p.Connection,1); % the number of elements
    p.FixedDOF = 1:6*p.SpokesNo;
% Fixes all the DoFs that are connected to the outer rim.
```

```
    p.Y = 0.01550;
% distance from centroid to strain gauge location along local y axis
    p.Z = 0.01796;
% distance from centroid to strain gauge location along local z axis

    p.SpokeArea = 0.00081866; % cross sectional area of beam in m^2
    p.MoAZ = 160.61217e-9;
% Moment of inertia about local Z axis of spoke in m^4
    p.MoAY = 110.27280e-9;
% Moment of inertia about local Y axis of spoke in m^4
    p.PMoI = p.MoAZ + p.MoAY; % Polar moment of inertia J in m^4

    p.YoungsModulus = 69e9; % in N/m^2 (Pa)
    p.ShearModulus = 26e9; % in N/m^2 (Pa)

    p.NodeCoordinates = [   OuterRimDiameter*cos(theta)/2
OuterRimDiameter*sin(theta)/2
0; % node 1
                            OuterRimDiameter*cos(theta+2*pi/5)/2
OuterRimDiameter*sin(theta+2*pi/5)/2
0; % node 2
                            OuterRimDiameter*cos(theta+4*pi/5)/2
OuterRimDiameter*sin(theta+4*pi/5)/2
0; % node 3
                            OuterRimDiameter*cos(theta+6*pi/5)/2
OuterRimDiameter*sin(theta+6*pi/5)/2
0; % node 4
                            OuterRimDiameter*cos(theta+8*pi/5)/2
OuterRimDiameter*sin(theta+8*pi/5)/2
0; % node 5
                            InnerHubDiameter*sin(4.5*pi+theta-beta)/2
InnerHubDiameter*cos(3.5*pi+theta-beta)/2
0; % node 6
                            InnerHubDiameter*sin(4.5*pi+theta-beta+2*pi/5)/2
InnerHubDiameter*cos(3.5*pi+theta-beta+2*pi/5)/2
0; % node 7
                            InnerHubDiameter*sin(4.5*pi+theta-beta+4*pi/5)/2
InnerHubDiameter*cos(3.5*pi+theta-beta+4*pi/5)/2
0; % node 8
```

```
                            InnerHubDiameter*sin(4.5*pi+theta-beta+6*pi/5)/2
InnerHubDiameter*cos(3.5*pi+theta-beta+6*pi/5)/2
0; % node 9
                            InnerHubDiameter*sin(4.5*pi+theta-beta+8*pi/5)/2
InnerHubDiameter*cos(3.5*pi+theta-beta+8*pi/5)/2   0; % node 10
                            0 0 0]; % node 11
% coordinate of each node in x1 y1 z1; x2 y2 z2; ....

elseif strcmp(text,'7 spoke FW') % 7 Spoke FW Inputs
    OuterRimDiameter = 0.38210; % in m
    InnerHubDiameter = 0.13965; % in m
    beta = (19) * pi/180;
% angle of spoke from line between center node to outer rim node
    p.SpokesNo = 7;
    p.Connection = [1 8;2 9;3 10;4 11;5 12;6 13;7 14;
8 15;9 15;10 15;11 15;12 15;13 15;14 15];
% shows which nodes are connected via elements
    p.ElementNo = size(p.Connection,1);
% the number of elements
    p.FixedDOF = 1:6*p.SpokesNo;
% Fixes all the DoFs that are connected to the outer rim.

    p.Y = 0.00511;
% distance from centroid to strain gauge location along local y axis
    p.Z = 0.01957;
% distance from centroid to strain gauge location along local z axis

    p.SpokeArea = 0.00022937;
% cross sectional area of beam in m^2
    p.MoAZ = 4.46988e-09;
% Moment of inertia about local Z axis of spoke in m^4
    p.MoAY = 43.4342e-09;
% Moment of inertia about local Y axis of spoke in m^4
    p.PMoI = p.MoAZ + p.MoAY;
% Polar moment of inertia J in m^4

    p.YoungsModulus = 45e9; % in N/m^2 (Pa)
    p.ShearModulus = 17e9; % in N/m^2 (Pa)
```

```
    p.NodeCoordinates = [   OuterRimDiameter*cos(theta)/2
                          OuterRimDiameter*sin(theta)/2
0; % node 1
                              OuterRimDiameter*cos(theta+2*pi/7)/2
OuterRimDiameter*sin(theta+2*pi/7)/2
0; % node 2
                              OuterRimDiameter*cos(theta+4*pi/7)/2
OuterRimDiameter*sin(theta+4*pi/7)/2
0; % node 3
                              OuterRimDiameter*cos(theta+6*pi/7)/2
OuterRimDiameter*sin(theta+6*pi/7)/2
0; % node 4
                              OuterRimDiameter*cos(theta+8*pi/7)/2
OuterRimDiameter*sin(theta+8*pi/7)/2
0; % node 5
                              OuterRimDiameter*cos(theta+10*pi/7)/2
OuterRimDiameter*sin(theta+10*pi/7)/2
0; % node 6
                              OuterRimDiameter*cos(theta+12*pi/7)/2
OuterRimDiameter*sin(theta+12*pi/7)/2
0; % node 7
                              InnerHubDiameter*sin(4.5*pi+theta-beta)/2
InnerHubDiameter*cos(3.5*pi+theta-beta)/2
0; % node 8
                              InnerHubDiameter*sin(4.5*pi+theta-beta+2*pi/7)/2
InnerHubDiameter*cos(3.5*pi+theta-beta+2*pi/7)/2
0; % node 9
                              InnerHubDiameter*sin(4.5*pi+theta-beta+4*pi/7)/2
InnerHubDiameter*cos(3.5*pi+theta-beta+4*pi/7)/2
0; % node 10
                              InnerHubDiameter*sin(4.5*pi+theta-beta+6*pi/7)/2
InnerHubDiameter*cos(3.5*pi+theta-beta+6*pi/7)/2
0; % node 11
                              InnerHubDiameter*sin(4.5*pi+theta-beta+8*pi/7)/2
InnerHubDiameter*cos(3.5*pi+theta-beta+8*pi/7)/2
0; % node 12
                              InnerHubDiameter*sin(4.5*pi+theta-beta+10*pi/7)/2
InnerHubDiameter*cos(3.5*pi+theta-beta+10*pi/7)/2
0; % node 13
```

```
                            InnerHubDiameter*sin(4.5*pi+theta-beta+12*pi/7)/2
InnerHubDiameter*cos(3.5*pi+theta-beta+12*pi/7)/2
0; % node 14
                            0 0 0]; % node 15

elseif strcmp(text,'9 split spoke ORW') % 9 Split Spoke ORW Inputs
    OuterRimDiameter = 0.39997; % in m
    InnerHubDiameter = 0.11726; % in m
    beta = 44.53*pi/180;
% angle between the secondary spoke and the primary spoke of the same psi fork
    SecondarySpokeLength = 0.14499*2; % in m
    p.SpokesNo = 9;
    p.Connection = [1 10;2 10;3 11;4 11;5 11;6 12;7 12;8 12;9 10;10 13;11 13;12 13];
% shows which nodes are connected via elements
    p.ElementNo = size(p.Connection,1);
% the number of elements
    p.FixedDOF = 1:6*p.SpokesNo;
% Fixes all the DoFs that are connected to the outer rim.

    p.Y = 0.01340;
% distance from centroid to strain gauge location along local y axis
    p.Z = 0.00829;
% distance from centroid to strain gauge location along local z axis

    p.SpokeArea = 0.00041984;
% cross sectional area of beam in m^2
    p.MoAZ = 22.394e-09;
% Moment of inertia about local Z axis of spoke in m^4
    p.MoAY = 34.584e-09;
% Moment of inertia about local Y axis of spoke in m^4
    p.PMoI = p.MoAZ + p.MoAY;
% Polar moment of inertia J in m^4

    p.YoungsModulus = 45e9; % in N/m^2 (Pa)
    p.ShearModulus = 17e9; % in N/m^2 (Pa)

    p.NodeCoordinates = [   OuterRimDiameter*cos(theta)/2
                        OuterRimDiameter*sin(theta)/2
                        0; % node 1
```

```
                            InnerHubDiameter*cos(theta)/2
+SecondarySpokeLength*cos(theta+beta)/2
InnerHubDiameter*sin(theta)/2
+SecondarySpokeLength*sin(theta+beta)/2
0; % node 2
                            InnerHubDiameter*cos(theta+2*pi/3)/2
+SecondarySpokeLength*cos(theta-beta+2*pi/3)/2
InnerHubDiameter*sin(theta+2*pi/3)/2
+SecondarySpokeLength*sin(theta-beta+2*pi/3)/2
0; % node 3
                            OuterRimDiameter*cos(theta+2*pi/3)/2
OuterRimDiameter*sin(theta+2*pi/3)/2
0; % node 4
                            InnerHubDiameter*cos(theta+2*pi/3)/2
+SecondarySpokeLength*cos(theta+beta+2*pi/3)/2
InnerHubDiameter*sin(theta+2*pi/3)/2
+SecondarySpokeLength*sin(theta+beta+2*pi/3)/2
0; % node 5
                            InnerHubDiameter*cos(theta+4*pi/3)/2
+SecondarySpokeLength*cos(theta-beta+4*pi/3)/2
InnerHubDiameter*sin(theta+4*pi/3)/2
+SecondarySpokeLength*sin(theta-beta+4*pi/3)/2
0; % node 6
                            OuterRimDiameter*cos(theta+4*pi/3)/2
OuterRimDiameter*sin(theta+4*pi/3)/2
0; % node 7
                            InnerHubDiameter*cos(theta+4*pi/3)/2
+SecondarySpokeLength*cos(theta+beta+4*pi/3)/2
InnerHubDiameter*sin(theta+4*pi/3)/2
+SecondarySpokeLength*sin(theta+beta+4*pi/3)/2
0; % node 8
                            InnerHubDiameter*cos(theta)/2
+SecondarySpokeLength*cos(theta-beta)/2
InnerHubDiameter*sin(theta)/2
+SecondarySpokeLength*sin(theta-beta)/2
0; % node 9
                            InnerHubDiameter*cos(theta)/2
InnerHubDiameter*sin(theta)/2
0.020; % node 10
```

```
                            InnerHubDiameter*cos(theta+2*pi/3)/2
InnerHubDiameter*sin(theta+2*pi/3)/2
0.020; % node 11
                            InnerHubDiameter*cos(theta+4*pi/3)/2
InnerHubDiameter*sin(theta+4*pi/3)/2
0.020; % node 12
                            0 0 0.020];
end

p.NodeNo = size(p.NodeCoordinates,1);
% counts the number of nodes

p.Xcoord = p.NodeCoordinates(:,1);
% co-ordinates of each node
p.Ycoord = p.NodeCoordinates(:,2);
p.Zcoord = p.NodeCoordinates(:,3);

p.GDOF = 6*p.NodeNo;
% total DoF, i.e. No of DoF of Node * No of nodes

% Zero Matrixes

p.Displacements = zeros(p.GDOF,1);
p.Force = zeros(p.GDOF,1);
p.Stiffness = zeros(p.GDOF,p.GDOF);

end
```

Global Stiffness Matrix

```
function StiffnessMatrix = GlobalStiffnessMatrix( p )
%StiffnessMatrix - Global stiffness for 3D Frame, constructed with Euler
%                  Bernoulli beam elements

StiffnessMatrix = zeros(p.GDOF);
```

```
E = p.YoungsModulus;
A = p.SpokeArea;
Iy = p.MoAY;
Iz = p.MoAZ;
G = p.ShearModulus;
J = p.PMoI;

for i = 1:p.ElementNo;
    CurrentElement = p.Connection(i,:);
% lists nodes that are connected to element of interest
    ElementDOF = [  CurrentElement(1)*6-5
                CurrentElement(1)*6-4
                CurrentElement(1)*6-3
                CurrentElement(1)*6-2
                CurrentElement(1)*6-1
                CurrentElement(1)*6
                CurrentElement(2)*6-5
                CurrentElement(2)*6-4
                CurrentElement(2)*6-3
                CurrentElement(2)*6-2
                CurrentElement(2)*6-1
                CurrentElement(2)*6];
    % degrees of freedom associated with the nodes of the current elemenmt

    X = p.Xcoord( CurrentElement(2), 1) - p.Xcoord( CurrentElement(1), 1);
% get difference in X, Y, Z coordinates of nodes
    Y = p.Ycoord( CurrentElement(2), 1) - p.Ycoord( CurrentElement(1), 1);
    Z = p.Zcoord( CurrentElement(2), 1) - p.Zcoord( CurrentElement(1), 1);

    L = sqrt(X*X + Y*Y + Z*Z); % pythagaros

    % stiffnesses of the degrees of freedom in local coordinates
    k1 = E*A/L;
    k2 = 12*E*Iz/(L*L*L);
    k3 = 6*E*Iz/(L*L);
    k4 = 4*E*Iz/L;
    k5 = 2*E*Iz/L;
    k6 = 12*E*Iy/(L*L*L);
    k7 = 6*E*Iy/(L*L);
```

```
    k8 = 4*E*Iy/L;
    k9 = 2*E*Iy/L;
    k10 = G*J/L;

    a = [k1 0 0;
         0 k2 0;
         0 0 k6];
    b = [0 0 0;
         0 0 k3;
         0 -k7 0];
    c = [k10 0 0;
          0 k8 0;
          0 0 k4];
    d = [-k10 0 0;
           0 k9 0;
           0 0 k5];

    k = [a   b   -a   b;
         b'  c    b   d;
       (-a)' b'   a  -b;
         b'  d' (-b)' c]; % stiffness matrix in local coordinates

    if i > p.SpokesNo
        k = k*1;
    end

    if X == 0 && Y == 0
% if true then CZZ = 0,
%then when calculating remaining transformations results in division by zero error.
        if Z > 0
            temp = [0 0 1 ; 0 1 0 ; -1 0 0];
        else
            temp = [0 0 -1 ; 0 1 0 ; 1 0 0];
        end
    else
        CXX = X/L; % transformation from x local to x global
        CYX = Y/L; % transformation from y local to x global
        CZX = Z/L; % transformation from z local to x global
```

```
        CZZ = sqrt(CXX*CXX + CYX*CYX);  % transformation from z local to z global

        CXY = -CYX/CZZ; % transformation from x local to y global
        CYY = CXX/CZZ; % transformation from y local to y global
        CZY = 0; % transformation from z local to y global
        CXZ = -CXX*CZX/CZZ; % transformation from x local to z global
        CYZ = -CYX*CZX/CZZ; % transformation from y local to z global

        temp = [CXX CYX CZX ;CXY CYY CZY ;CXZ CYZ CZZ];
    end

    R = [temp zeros(3,9);
        zeros(3) temp zeros(3,6);
        zeros(3,6) temp zeros(3);
        zeros(3,9) temp];
% 3D transformation matrix for 2-node bernoulli beam element

    StiffnessMatrix(ElementDOF,ElementDOF) =
StiffnessMatrix(ElementDOF,ElementDOF) + R'*k*R;
            % converts stiffness matrix from local to global coordinates
            % add stiffness matrix to overall matrix in
%location of corresponding degrees of freedom
end


end
```

Solution of Structure

```
function displacements = SolutionOfStructure( p )
%SolutionOfStructure
%   Calculates solution of global displacements
ActiveDOF = setdiff([1:p.GDOF]',[p.FixedDOF]); % the nodes which allow movement

U = p.Stiffness(ActiveDOF,ActiveDOF) \ p.Force(ActiveDOF); % calculate displacements
```

```
displacements = zeros(p.GDOF,1);
displacements(ActiveDOF) = U; % returning only active degrees of freedom

end
```

Calculating strain on primary spoke

```
function Strain = CalculateStressForPrimarySpoke( p , Xcoordinate )
%Strain -   the strain at the primary element at x location on y/z surface
%           Calculate the strain in the first element within a 3D frame
%           p           variable structure containing wheel details
%           direction   direction, in local coordinate system, to surface on
%                       spoke of interest [y or z]
%           Xcoordinate location of strain gauge along local x coordinate [m]

%Calculates strain from:
%                   e_xx = Normal Strain = B d assumes plane strain
%                   B = Strain Displacement Matrix
%                   d = Displacements

CurrentElement = p.Connection(1,:);
% lists nodes that are connected to element of interest
ElementDOF = [  CurrentElement(1)*6-5
CurrentElement(1)*6-4
CurrentElement(1)*6-3
CurrentElement(1)*6-2
CurrentElement(1)*6-1
CurrentElement(1)*6
CurrentElement(2)*6-5
CurrentElement(2)*6-4
CurrentElement(2)*6-3
CurrentElement(2)*6-2
CurrentElement(2)*6-1
CurrentElement(2)*6];
% degrees of freedom associated with the nodes of the current elemenmt

X = p.Xcoord( CurrentElement(2)) - p.Xcoord( CurrentElement(1));
```

```
% get difference in X, Y, Z coordinates of nodes
Y = p.Ycoord( CurrentElement(2)) - p.Ycoord( CurrentElement(1));
Z = p.Zcoord( CurrentElement(2)) - p.Zcoord( CurrentElement(1));

L = sqrt(X*X + Y*Y + Z*Z); % pythagaros

if X == 0 && Y == 0
% if true then CZZ = 0,
%then when calculating remaining transformations results in division by zero error.
    if Z > 0
        temp = [0 0 1 ; 0 1 0 ; -1 0 0];
    else
        temp = [0 0 -1 ; 0 1 0 ; 1 0 0];
    end
else
    CXX = X/L; % transformation from x local to x global
    CYX = Y/L; % transformation from y local to x global
    CZX = Z/L; % transformation from z local to x global

    CZZ = sqrt(CXX*CXX + CYX*CYX);  % transformation from z local to z global

    CXY = -CYX/CZZ; % transformation from x local to y global
    CYY = CXX/CZZ; % transformation from y local to y global
    CZY = 0; % transformation from z local to y global
    CXZ = -CXX*CZX/CZZ; % transformation from x local to z global
    CYZ = -CYX*CZX/CZZ; % transformation from y local to z global

    temp = [CXX CYX CZX ;CXY CYY CZY ;CXZ CYZ CZZ];
end

R = [temp zeros(3,9);
    zeros(3) temp zeros(3,6);
    zeros(3,6) temp zeros(3);
    zeros(3,9) temp];
% 3D transformation matrix for 2-node bernoulli beam element

u = p.Displacements(ElementDOF);
% Displacements of the element of interest in global coordinates
ue = R*u; % Displacements in local coordinates
```

```
B = [-1/L
(6/L^2-12*Xcoordinate/L^3)*p.Y
p.Z*(-6/L^2+12*Xcoordinate/L^3)
0
(-4/L+6*Xcoordinate/L^2)*p.Z
p.Y*(4/L-6*Xcoordinate/L^2)
1/L
(-6/L^2+12*Xcoordinate/L^3)*p.Y
p.Z*(6/L^2-12*Xcoordinate/L^3)
0
(-2/L+6*Xcoordinate/L^3)*p.Z
(2/L-6*Xcoordinate/L^3)*p.Y];

Strain = (B * ue);

end
```

ASME Factor of Safety

```
function [VonMisesASMEn, PrincipleASMEn] = AppliedStresses( p , division)

VonMises = zeros(division,3);
VonMises = p.Strain(:,1);
Principle = zeros(division,6);
Principle = p.Strain(:,1);

% Calculate the Von Mises and Principle stresses at each orientation
for i = 0:division

    %Strains in X, Y, Z directions
    Epsilon_x = p.Strain(i+1,2);
    Epsilon_y = -1 * p.PoisonRatio * Epsilon_x;
    Epsilon_z = -1 * p.PoisonRatio * Epsilon_x;

    %Stresses in X, Y, Z directions
    Sigma_x = p.YoungsModulus*Epsilon_x;
```

```
    Sigma_y = p.YoungsModulus*Epsilon_y;
    Sigma_z = p.YoungsModulus*Epsilon_z;

    %Shear stresses in X, Y, Z directions
    Tau_xy = p.ShearModulus*p.Theta_x(i+1,2);
    Tau_yz = 0;
    Tau_zx = 0;

    %Von Mises stress
    VonMises(i+1,2) = VonMisesStress(Sigma_x, Sigma_y, Sigma_z,
Tau_xy, Tau_yz, Tau_zx);
    %Von Mises Safety Factor
    VonMises(i+1,3) = abs(p.YieldStrength/VonMises(i+1,2));

    %Principle stress
    PrincipleTemp = sort(PrincipleStress(Sigma_x, Sigma_y, Sigma_z,
Tau_xy, Tau_yz, Tau_zx));

    Principle(i+1,2) = PrincipleTemp(3); %Max Principle Stress sigma_1
    Principle(i+1,3) = PrincipleTemp(2); %Middle Principle Stress sigma_2
    Principle(i+1,4) = PrincipleTemp(1); %Min Principle Stress sigma_3
    %First yield safety factor (Max)
    Principle(i+1,5) = abs(p.YieldStrength/Principle(i+1,2));
    %First yield safety factor (Min)
    Principle(i+1,6) = abs(p.YieldStrength/Principle(i+1,4));

end

%ASME fatigue factor of safety using Von Mises max/min
MaxVonMises = max(VonMises(:,2));
MinVonMises = min(VonMises(:,2));
VonMisesMean = (MaxVonMises+MinVonMises)/2;
VonMisesAlt = abs((MaxVonMises-MinVonMises)/2);
VonMisesASMEn = ASMESafetyFactor(VonMisesMean, VonMisesAlt,
p.EnduranceStrength, p.YieldStrength);

%ASME fatigue factor of safety using Principle max/min
MaxPrinciple = max(Principle(:,2));
MinPrinciple = min(Principle(:,4));
```

```
PrincipleMean = (MaxPrinciple+MinPrinciple)/2;
PrincipleAlt = abs((MaxPrinciple-MinPrinciple)/2);
PrincipleASMEn = ASMESafetyFactor(PrincipleMean, PrincipleAlt,
p.EnduranceStrength, p.YieldStrength);

end

function sigma_m = VonMisesStress(Sigma_x, Sigma_y, Sigma_z, Tau_xy, Tau_yz, Tau_zx)
%Calculate the Von Mises stress using formula on Shigley's (pg 215)
temp = power(Sigma_x-Sigma_y,2) + power(Sigma_y-Sigma_z,2) + power(Sigma_z-Sigma_x,2)
+ 6*(power(Tau_xy,2)+power(Tau_yz,2)+power(Tau_zx,2));
sigma_m = power(temp,0.5)/sqrt(2);

end

function principle = PrincipleStress(Sigma_x, Sigma_y, Sigma_z,
Tau_xy, Tau_yz, Tau_zx)
%Calculate the principle stress using formula on Shigly's (pg 83)
a = 1;
b = Sigma_x + Sigma_y + Sigma_y;
c = Sigma_x*Sigma_y + Sigma_x*Sigma_z + Sigma_y*Sigma_z - power(Tau_xy,2)
- power(Tau_yz,2) - power(Tau_zx,2);
d = Sigma_x*Sigma_y*Sigma_z + 2*Tau_xy*Tau_yz*Tau_zx - Sigma_x*power(Tau_yz,2)
- Sigma_y-power(Tau_zx,2) - Sigma_z-power(Tau_xy,2);
coefficients = [a b c d];
principle = roots(coefficients);

end

function ASMEn = ASMESafetyFactor(Sigma_mean, Sigma_alt,
EnduranceStrength, YieldStrength)
%Calculate the ASME safety factor using the formula on Shigly's (pg 215)
temp = power(Sigma_alt/EnduranceStrength,2) + power(Sigma_mean/YieldStrength,2);
ASMEn = power(temp, -0.5);

end
```

Main Program

```
%Program solves reaction forces, global displacements and strains
%               for a wheel design (approximated by a 3D frame),
%               by discretising each spoke into an euler-bernoulli element.
%               Increases theta from 0 to 360 degrees then outputs the
%               strain
%Written by:    Brandon Heukelman

% Number of points in 360 degree loop to evaluate strain
division = 90;

% Select which wheel inputs to load
TestWheel = '7 spoke FW';
%TestWheel = '5 spoke CRW';
%TestWheel = '9 split spoke ORW';

% Local x coordinate on spoke to evaluate strain
localXcoord = 0.08905;

% Forces and moments acting at center node
FX = +300*9.81*cos(8.75*pi/180);
FY = 0;
FZ = -300*9.81*sin(8.75*pi/180);
MX = 0;
MY = -300*9.81*0.4586;
MZ = 0;

% Creating variables of appropriate size
strain = zeros(division,2);
theta_x = zeros(division,2);

% Increase theta from 0 to 360 degrees
for i = 0:division
    theta = i*(360/division)*pi/180;

    % Load inputs and coordinates for wheel
    Wheel = WheelInputs(TestWheel, theta);
```

```
    % Creates global stiffness matrix from each element
    Wheel.Stiffness = GlobalStiffnessMatrix(Wheel);

    % Assign forces to appropriate node and degree of freedom
    Wheel.Force((length(Wheel.Connection)*6)+1) = FX;
    Wheel.Force((length(Wheel.Connection)*6)+2) = FY;
    Wheel.Force((length(Wheel.Connection)*6)+3) = FZ;
    Wheel.Force((length(Wheel.Connection)*6)+4) = MX;
    Wheel.Force((length(Wheel.Connection)*6)+5) = MY;
    Wheel.Force((length(Wheel.Connection)*6)+6) = MZ;

    % Solve system, returns global displacements
    Wheel.Displacements = SolutionOfStructure(Wheel);

    % Store angle of twist of spoke along longitudinal axis (local x)
    theta_x(i+1,1) = theta*180/pi;
    theta_x(i+1,2) = Wheel.Displacements(46);

    % Calculate strains for primary spoke
    strain(i+1,1) = theta*180/pi;
    strain(i+1,2) = SolutionOfStrain(Wheel, localXcoord);
end

% Store strain and angle of twist
Wheel.Strain = strain;
Wheel.Theta_x = theta_x;

% Calculate the ASME factor of safety
AppliedStresses(Wheel, division);
```